ELSEVIER

Materials Science and Engineering B87 (2001) 1–22

MATERIALS SCIENCE & ENGINEERING B

www.elsevier.com/locate/mseb

Review

Real-time optical characterization of thin film growth

N. Dietz *

Department of Physics and Astronomy, Georgia State University, Atlanta, GA 30303, USA

Accepted 21 June 2001

Abstract

The further spatial reduction together with stringent thickness and composition tolerances in manufacturing of advanced electronic and optical devices require new approaches to control the growth process as well as to improve the insight into the deposition process itself. The development of non-invasive, real-time, structure-specific analytical tools for characterizing phenomena occurring at surfaces and interfaces during thin film growth has therefore to address both, providing a detailed understanding of the thin film growth process and providing robust process control signals in real-time. This review gives an overview of the principles of angle resolved reflectance techniques applied to real-time thin film process monitoring, the study of surface reaction kinetics, and to growth process control. The capabilities of high-sensitive thin film growth monitoring and control are illustrated for the growth of III-V compounds under pulsed chemical beam epitaxy conditions, using p-polarized reflectance spectroscopy as an example. © 2001 Published by Elsevier Science B.V.

Keywords: Optical characterization; Thin film growth; Chemical beam epitaxy

1. Introduction

The development of surface-sensitive real-time optical characterization techniques that are able to give insights in the surface reaction kinetics during deposition or etching processes are essential for further progress in understanding and controlling such processes. For example, the defect formation and the interactions/propagation during heteroepitaxial growth requires the understanding and control of the kinetics of heteroepitaxy, which is closely related to surface structure that depends on both reconstruction and the nature and distribution of defects in the epitaxial film. Even though, reduced pressure deposition methods such as organometallic chemical vapor deposition (OMCVD), chemical beam epitaxy (CBE), or plasma enhanced chemical vapor deposition play an important role in manufacturing, the progress in understanding and controlling these processes has been very slow, considering how limited our knowledge is about chemical reaction pathways, the reaction kinetics during the decomposition process of organometallic precursors, or the correlation to defect formation in the growth of compound semiconductors. In addition, the stringent tolerances in the engineering of advanced optoelectronic integrated circuits with respect to control thickness and composition of ultra-thin layers require the development of monitoring and control techniques that follow the deposition process with sub-monolayer resolution [1].

Optical characterization techniques are becoming important tools for in-situ or real-time monitoring in materials research with advances particularly in the areas of non-intrusive thin film characterization and process control. However, optical probes have several well-know limitations regarding the spectral wavelength range accessible, sensitivity towards surface processes, or their complexity in implementation and/or interpretation. Most reflectance-based techniques such as dynamic optical reflectivity (DOS) [2–4], spectral resolved normal incidence reflectance spectroscopy (NRIS) [5,6] or pyrometric interferometry (PI) [7] are successfully applied to various deposition processes and provide information on both the growth rate and the composi-

---

* Tel.: + 1-404-463-9617; fax: + 1-404-651-3419.
E-mail address: ndietz@gsu.edu (N. Dietz).

0921-5107/01/$ - see front matter © 2001 Published by Elsevier Science B.V.
PII: S0921-5107(01)00711-5

tion of the deposits, however, they are relatively insensitive to surface processes that drive deposition or etching processes.

The sensitivity of optical probe techniques is determined approximately by the ratio of the penetration depth of light to the thickness of the surface layer, which is for CBE/OMCVD processes in the order of 100:1. Thus the reflected beam carries roughly 99% bulk and only 1% surface relevant information. Taking into account light source instabilities (typically $<1\%$) and detector limitation (noise and dynamic range), signal contributions smaller than 1% are hardly to resolve by standard reflectance/transmission techniques.

The urge to gain a better understanding to surface processes led to the development of surface-sensitive real-time optical sensor techniques [8] such as reflectance-difference spectroscopy (RDS) [1,9–11], surface photo absorption (SPA) [12–14], p-polarized reflectance spectroscopy (PRS) [15–17] and laser light scattering (LLS) [18], which are providing new insights into surface chemistry and surface reconstruction and surface morphology during growth. Those techniques are able to characterize and monitor surface processes in the vicinity where the growth occurs, which, for example, in a CBE process is the surface reaction layer (SRL), built up of physisorbed and chemisorbed precursor fragments between the ambient and film interface.

However, applying optical probe techniques towards real-time characterization of thin film growth also inherits the challenge to relate surface chemistry processes that drives the growth process, towards growth/film properties, such as composition, instantaneous growth rate or structural layer quality. As illustrated in Fig. 1, in deposition four primary regions are involved. Presently, most characterization techniques are being directed towards accurately measuring ambient process parameters, such as pressure, flux or temperature, since numerous probes are available to provide a relative detailed assessment of the ambient. This strategy is clearly limited in its capability to deal with complex nonlinear surface chemistry processes, where the surface plays an integral role in the precursor decomposition pathways and small changes in the ambient composition can affect the growth substantially.

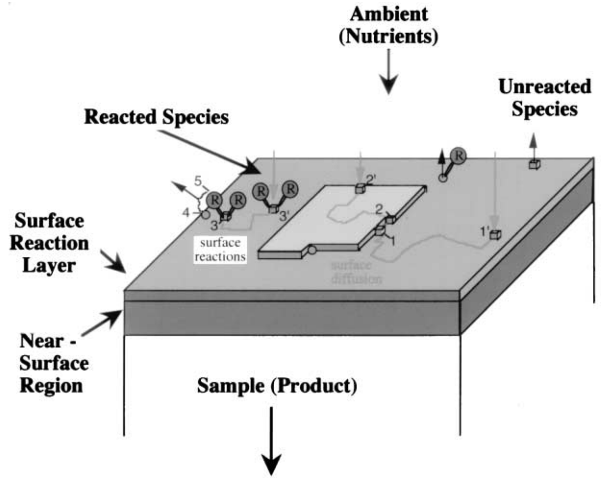

Fig. 1. The four primary regions involved in deposition are: (1) the ambient; (2) the surface reaction layer, which consists of species physisorbed or chemisorbed to the surface in dynamic equilibrium with both ambient and surface; (3) the surface itself; and (4) the near-surface region that can be defined as consisting of the outermost several atomic layers of the fabricated sample.

The development of diagnostic tools that are based on interaction of light with mater gaining increasingly of importance for industrial applications in communications, process control, environmental pollution monitoring and medical diagnostics. These type of devices are based in one way or the other on the analysis of the light before and after the interaction with matter in order to gain information about the matter itself—or—to changes at the interfaces of ambient or matters. Also, the use of optical sensors for the real-time monitoring of etching and/or growth processes is favored because of their non-destructive character and some of these methods are ideal to monitor the overall growth process and/or substrate temperature in industrial applications, requiring low cost and maintenance.

The following chapters briefly summarize the physical principles on which reflectance methods are based. The review is focusing on angle resolved reflectance techniques and in particular pseudo-Brewster angle reflectance configuration techniques applied to thin film process characterization or the study of surface reaction kinetics. In the last section, the use of PRS for thin film growth monitoring and control will be discussed.

2. Reflectance methods

The electromagnetic radiation interacting with matter can be described either as an electromagnetic wave that is defined by electric and magnetic field oscillating with the frequency ν, or as a photon (quantized particle) with an energy $\hbar\omega$. For the detection diagnostics described here, the wave picture of light is sufficient for the description of the interaction process and only the matter will be treated quantum mechanically. Comprehensive descriptions of optics and applications of optics can be found in the works by Born and wolf [19], Azzam and Bashara [20], Herman [21] and Bauer [22]. The notation used here complies with the 'Nebraska optical conventions' [20] and all expressions are given in MKSA (SI) units.

An incidence plane wave front traveling in the x–z-plane in $\vec{k}_1$-direction with the velocity v_1 (see Fig. 2), in an orthogonal coordinate system can be represented as

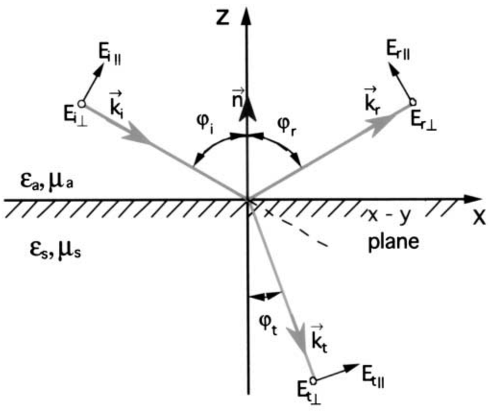

Fig. 2. Schematic propagation of a plane electromagnetic wave in the $z-x$ plane, refracted and reflected at an interface laying in the x–y plane.

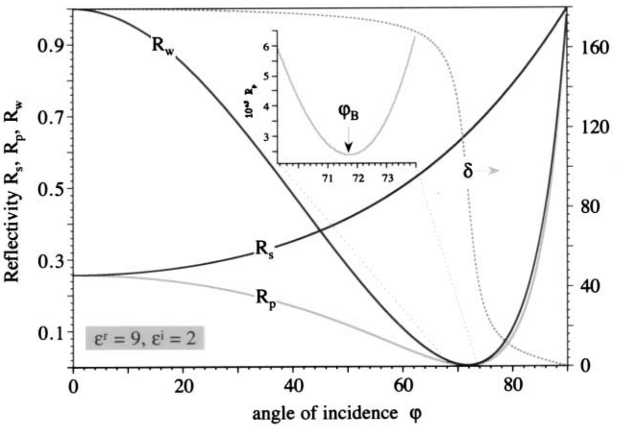

Fig. 3. Angle dependency of phase and reflectivity of p-, s-polarized light on a single interface ambient-substrate.

$$\vec{E}_i(\vec{r},t) = \begin{pmatrix} E_{i\|} \cos \varphi_i \\ E_{i\perp} \\ E_{i\|} \sin \varphi_i \end{pmatrix} e^{i\omega(t-(x \sin \varphi_i - z \ \cos \varphi_i/v_v))}, \qquad (2.1)$$

where φ_i denotes the angle of incidence and $E_{i\|}$, $E_{i\perp}$ are the complex field coefficients describing the amplitude and phase dependencies parallel and perpendicular to the plane of incidence, which is defined as by the incidence wave and the normal vector perpendicular to the surface. The Fresnel equations can be derived from the continuum conditions at the boundary using Maxwell's equations for radiation propagating through an uncharged homogenous medium having the permeability μ, a dielectric function ε, and an electrical conductivity σ.

The continuum boundary conditions at an interface result for the parallel (p) and perpendicular (s) electrical field vectors of the incident, refracted and reflected beam components in the Fresnel's transmittance (t) and reflectance (r) coefficients [23]:

$$t_s = \frac{|E_{t_o}|}{|E_{i_o}|}\bigg|_{E_\perp} = \frac{2 \cos \varphi_i \sqrt{\mu_a \varepsilon_a}}{\sqrt{\mu_a \varepsilon_a} \cos \varphi_i - \dfrac{\mu_a}{\mu_s} \sqrt{\mu_s \varepsilon_s - \mu_a \varepsilon_a \sin^2 \varphi_i}}, \qquad (2.2)$$

$$t_p = \frac{|E_{t_o}|}{|E_{i_o}|}\bigg|_{E_\|} = \frac{2 \cos \varphi_i \sqrt{\mu_a \varepsilon_a} \sqrt{\mu_s \varepsilon_s}}{\mu_a \varepsilon_s \cos \varphi_i + \sqrt{\mu_a \varepsilon_a} \sqrt{\mu_s \varepsilon_s - \mu_a \varepsilon_a \sin^2 \varphi_i}}, \qquad (2.3)$$

$$r_s = \frac{|E_{s_o}|}{|E_{i_o}|}\bigg|_{E_\perp} = \frac{\sqrt{\mu_a \varepsilon_a} \cos \varphi_i - \dfrac{\mu_a}{\mu_s} \sqrt{\mu_s \varepsilon_s - \mu_a \varepsilon_a \sin^2 \varphi_i}}{\mu_a \varepsilon_a \cos \varphi_i + \dfrac{\mu_a}{\mu_s} \sqrt{\mu_s \varepsilon_s - \mu_a \varepsilon_a \sin^2 \varphi_i}}, \qquad (2.4)$$

$$r_p = \frac{|E_{s_o}|}{|E_{i_o}|}\bigg|_{E_\|} = \frac{\mu_a \varepsilon_s \cos \varphi_i - \sqrt{\mu_a \varepsilon_a} \sqrt{\mu_s \varepsilon_s - \mu_a \varepsilon_a \sin^2 \varphi_i}}{\mu_a \varepsilon_s \cos \varphi_i + \sqrt{\mu_a \varepsilon_a} \sqrt{\mu_s \varepsilon_s - \mu_a \varepsilon_a \sin^2 \varphi_i}}, \qquad (2.5)$$

where indices s and p denote the perpendicular and parallel coefficient, respectively.

The relations between the complex refractive index $\hat{n} = n - \mathrm{i}\, k$ and the complex dielectric function $\varepsilon = \varepsilon^r - \mathrm{i}\varepsilon^i$ of a medium are given though the solution of the Maxwell's equations for a plane wave traveling in a medium having a electrical conductivity σ, the permeability μ, and a dielectric function ε by:

$$\hat{n}^2 = n^2 - k^2 - \mathrm{i}2nk = \frac{c^2}{v^2} - \frac{\mathrm{i}\sigma\mu c^2}{\omega} = \varepsilon = \varepsilon^r - \mathrm{i}\varepsilon^i, \qquad (2.6)$$

with

$$n = \sqrt{\frac{|\varepsilon| + \varepsilon^r}{2}}, k = \sqrt{\frac{|\varepsilon| - \varepsilon^r}{2}} \varepsilon^r = n^2 - k^2 = n^2 - \frac{\alpha^2 c^2}{4\omega^2} = \frac{c^2}{v^2},$$

and

$$\varepsilon^i = 2nk = \frac{\sigma\mu c^2}{\omega} = \frac{nc\alpha}{\omega}$$

where n denotes the real part of the refractive index, k the extinction coefficient, α the absorption coefficient, ω the frequency of the wave, v the velocity of the wave in a medium, and c denotes the speed of light.

The complex Fresnel's coefficients (Eqs. (2.2)–(2.5)) are expressed with respect to the angle of incidence φ_i, and the index i is not required for the further description. Also, for semiconductors considered here, we set the permeability $\mu = 1$, which further simplifies the equations.

The reflectivity of the electromagnetic wave vector polarized parallel (p) or perpendicular (s) to the plane of incidence are given by

$$R_p = r_p r_p^* \text{ and } R_s = r_s r_s^*, \qquad (2.7)$$

the angle dependency of which is shown in Fig. 3. Also shown is the reflectance ratio R_w defined by

$$R_\mathrm{w} = [\tan(\psi_\mathrm{r})]^2 = \left[\frac{|r_\mathrm{p}|}{|r_\mathrm{s}|}\right]^2, \tag{2.8}$$

and the phase shift δ, given by

$$\delta = \mathrm{atan}\left[\frac{2xy^2\sqrt{\frac{1}{2}(-\varepsilon^\mathrm{r} + y^2 + \sqrt{\varepsilon^{\mathrm{i}^2} + (\varepsilon^\mathrm{r} - y^2)^2})}}{-y^4 + x^2\sqrt{\varepsilon^{\mathrm{i}^2} + (\varepsilon^\mathrm{r} - y^2)^2}}\right], \tag{2.9}$$

The reflectivity for s-polarized light, R_s, increases monotone reaching unity for an angle of incidence $\varphi = 90°$, while the reflectivity for p-polarized light, R_p, first decreases, reaches a minimum and than increases to unity for $\varphi = 90°$. The inset in Fig. 3 shows an enlargement of R_p around the minimum.

Fig. 3 contains several features notable to be discussed. At normal incidence ($\varphi = 0$), the r_p and r_s reflectance coefficients are identical and the reflectivity and be written as

$$R = \left|\frac{\sqrt{\varepsilon} - 1}{\sqrt{\varepsilon} + 1}\right|^2 = \frac{(n-1)^2 + k^2}{(n+1)^2 + k^2}, \tag{2.10}$$

which for the case $k = \varepsilon^\mathrm{i} = \alpha = 0$ (no absorption) directly links the reflectivity to the refractive index n

$$n = \frac{1 + \sqrt{R}}{1 - \sqrt{R}}. \tag{2.11}$$

This relation is valid for any isotropic medium and any polarization direction of the incoming light. A similar relation we can obtain from the feature, which was first phenomenologically described by David Brewster [24] in 1813. He observed that for a transparent medium at a specific angle of incidence, called the Brewster angle φ_B, the reflectivity vanishes if light polarized parallel to plane of incidence is used. Formulating an extrema condition $r_\mathrm{P}|\varphi_\mathrm{B} = 0$ for Eq. (2.5) and assuming $\varepsilon^\mathrm{i} = 0$, we obtain

$$\varphi_\mathrm{B} = \arctan\sqrt{\varepsilon} = \arctan(n) \quad \text{or} \quad n = \tan\varphi_\mathrm{B}, \tag{2.12}$$

allowing to obtain the optical materials property via one observable.

For the more general case of $\varepsilon^\mathrm{i} \neq 0$, the extrema condition $r_\mathrm{P}|\varphi_\mathrm{B} = 0$ has to be modified to a minimum condition for R_p that can be analyzed by $\mathrm{d}(R_\mathrm{p}|\varphi_\mathrm{B})/\mathrm{d}\,\varphi = 0$ Miller [25] showed that for materials with small absorption ($k \ll 1$), the reflectivity R_p near the Brewster angle (see inset in Fig. 3) can be approximated by an quadratic function

$$R = R_0\left\{1 - \left(\frac{\eta}{\eta_0}\right)^2\right\}, \tag{2.13}$$

where R_0 is the minimum reflectivity and η is the deviation in the angle of incidence from that of the position of the minimum. An analytical expression for the minimum condition was formulated by Humphreys-Owen [26], which yielded in a cubic expression for $y_\mathrm{B}^2 = \sin^2\varphi_\mathrm{B}$ in the from of

$$y_\mathrm{B}^6(2|\varepsilon|^2 + 2\varepsilon^\mathrm{r}) + y_\mathrm{B}^4(|\varepsilon|^4 - 3|\varepsilon|^2) - 2y_\mathrm{B}^2|\varepsilon|^4 + |\varepsilon|^4 = 0. \tag{2.14}$$

The solution of this equation has several paths that can numerically be analyzed and correlated to physical allowable value ranges. Such a numerical evaluation showed that a general expression of the Brewster angle in the from [27]:

$$\varphi_\mathrm{B} = \arcsin\left[\sqrt{\frac{-|\varepsilon|^2}{3(|\varepsilon|^2 + \varepsilon^\mathrm{r})}\left[|\varepsilon|^2 - 3 + \cos\left(\frac{\chi}{3} + \frac{4\pi}{3}\right)\sqrt{|\varepsilon|^4 + 6|\varepsilon|^2 + 12\varepsilon^\mathrm{r} + 9}\right]}\right], \tag{2.15}$$

with

$$\cos\chi = \frac{|\varepsilon|^4[|\varepsilon|^8 + 9\varepsilon^6 + 27|\varepsilon|^4 + 18|\varepsilon|^4\varepsilon^\mathrm{r} - 27|\varepsilon|^2 + 54|\varepsilon|^2\varepsilon^\mathrm{r} + 54(\varepsilon^\mathrm{r})^2]}{\sqrt{(|\varepsilon|^4 + 6|\varepsilon|^2 + 12\varepsilon^\mathrm{r} + 9)^3}},$$

can be derivated, which reduces to the well-known Eq. (2.12) for the case of $\varepsilon^\mathrm{i} = 0$. For the generalized minimum condition, which includes any absorbing medium, the Brewster angle is also denoted as pseudo-Brewster angle or First Brewster angle [26,28,29]. The angle of incidence at which the polarization is a maximum and the reflectance ratio R_w a minimum, is denoted as the second Brewster angle. The third Brewster angle is defined by the condition where the phase shift δ is equal 90°. In the further discussion in this text, the term Brewster angle is used broadly including the condition described as pseudo-Brewster angle.

The above analysis of the Fresnel equations and reflectance coefficients are considered for an ambient-medium interface, where the optical density of the ambient is small than that of the medium. For instance, if optical fibers or rods are used to guide light beams to probing media/surfaces, the ambient dielectric function ε_a might be higher than the probed medium dielectric function ε_m. In such a case total reflectance will occur above the critical angle of total reflectance φ_c, which is defined by

$$\sin(\varphi_\mathrm{c}) = \frac{\sqrt{\varepsilon_\mathrm{m}}}{\sqrt{\varepsilon_\mathrm{a}}}; \quad (\varepsilon_\mathrm{a}\text{:ambient,}\varepsilon_\mathrm{m}\text{:medium}). \tag{2.16}$$

Note that the Brewster angle, $\tan(\varphi_\mathrm{B}) = \sqrt{\varepsilon}$, remains always smaller than the critical angle of total reflectance φ_c. The angle dependency of reflectance coefficients R_p and R_s is compressed in an angle range $(0<\varphi<\varphi_c)$, as shown in Fig. 4 for the example Sapphire (ambient)–air (medium) interface.

The reflectance ratio R_w (Eq. (2.8)) at a fixed angle of incidence, together with the phase shift δ (Eq. (2.9)) at this angle are the measurement values in an ellipsometric experiment. The link to the optical functions has been established early on and are given by:

$$\mathrm{Re}\{\varepsilon\}=\frac{\sin^2\varphi\,\tan^2\varphi[\cos^2(2\psi_r)-\sin^2(2\psi_r)\sin^2\delta]}{(1+\sin(2\psi_r)\cos\delta)^2}, \tag{2.17}$$

and

$$\mathrm{Im}\{\varepsilon\}=\frac{\sin^2\varphi\,\tan^2\varphi\,\sin^4(4\psi_r)\sin^2\delta}{(1+\sin(2\psi_r)\cos\delta)^2}.$$

Maximum sensitivity for ellipsometric measurements is observed for an angle of incidence chosen to be the second or third Brewster angle. However, any beam divergence would lead to a significant error in the determination of R_p and δ. In addition, the detector dynamic range has to be adjusted to accommodate small R_p as well as large R_s values with a sufficient signal-to-noise ratio. From these considerations, the angle of incident is chosen typically in the range between 60 and 67°, since most semiconductors under consideration, have a Brewster angle above 68° in the visible and ultraviolet wavelength regime. Typically, the incident beam is placed in a defined state of polarization by passing it through a linear polarizer, and the polarization state of the reflected beam determined by passing it through a rotating analyzer or photoelastic modulator. The principles of Ellipsometry and its application to materials and thin film characterization has been reviewed in several articles [30,31].

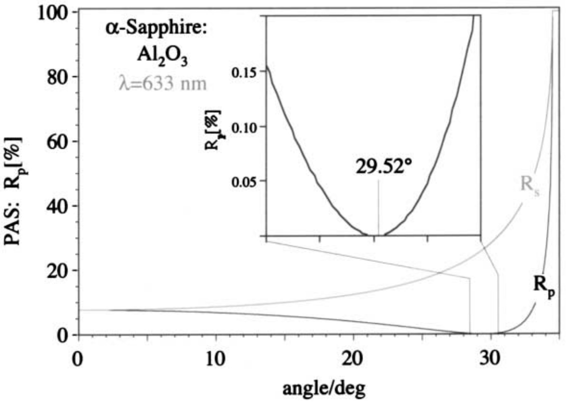

Fig. 4. Angle dependent reflection coefficients for p- and s-polarized light reflected from a sapphire ($\varepsilon=3.118$)/air ($\varepsilon=1.0$) interface.

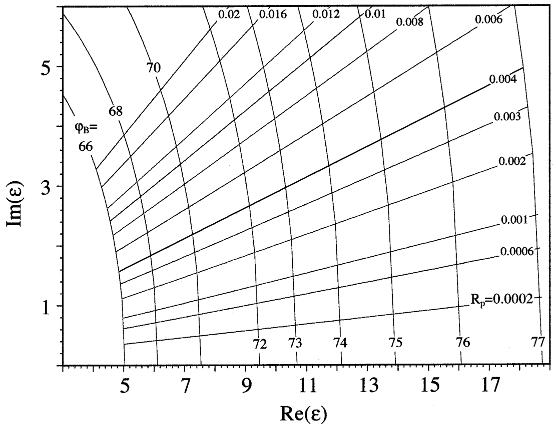

Fig. 5. Families of iso-R_p and iso-φ_B contours in the ε_1–ε_2 plane. R_p is the reflectivity at the Brewster angle φ_B for light, polarized parallel to the plane of incidence. The contour plot shows R_p and φ_B values typically encountered for semiconductors in the weak to medium absorbent regime.

Utilizing the Brewster angle as one of the measurement values for the determination the optical properties of a medium, four distinct measurement methods configuration have been proposed [26,32] and analytical expressions for the optical properties, $\varepsilon=f(\varphi_B,R)$ developed:

Method A: Brewster angle φ_B and reflectivity R_s at φ_B [26,28],

Method B: Brewster angle φ_B and reflectivity R_p at φ_B [26,27,33],

Method C: Brewster angle φ_B and reflectivity ratio (R_p/R_s) at φ_B [26], and

Method D: Brewster angle φ_B and reflectivity R_0 at normal incidence [34,35].

A significant disadvantage in the development of these techniques was the lack or complexity of analytical expressions linking the measured parameter to the optical functions, the development of which took till end of the 80th. For an evaluation of the usefulness of these techniques, several criteria have to be taken in account:

1. the sensitivity and accuracy to measure the optical properties,
2. the advantages compared to established optical techniques such as Ellipsometry or Reflectometry, and
3. experimental considerations such as complexity of sample alignment, dynamic range of detectors, noise limitations, moving/rotating parts, and time required to obtain the desired information.

Method D requires independent measurements at two different angle regimes, which is experimentally difficult to implement and time consuming to realize. Experimental setups for Methods A and C require the analyzation of the polarization state at either one or two angles of incidence. Since both methods have to evaluate the reflectivity for perpendicular polarized light, the detector dynamic range, typically between 10^3 and 10^4, has to be adjusted to the high s-polarized reflected intensity, driving the p-component in the noise level. No advantage in sensitivity and measurement

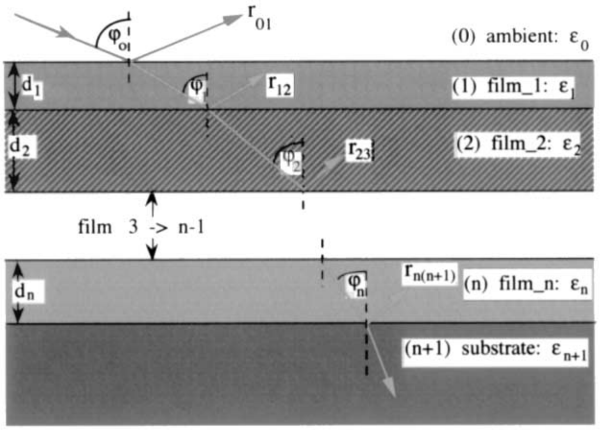

Fig. 6. Schematic illustration of the reflectance contributions from a multi-layer media (ambient/film_1 to film_*n*/substrate) for homogeneous isotropic media.

speed is gained compared to Ellipsometry, which is well established.

Method B, which analyzes φ_B and reflectivity R_p at φ_B, has the advantage of a nulling technique with a high sensitivity to any changes introduced by the wavelength dependency of the dielectrics function. Its application, proposed as Brewster angle spectroscopy (BAS) [27], was also successfully applied for radiative and non-radiative defect characterization in semiconductors [36]. The observed high sensitivity towards surface modifications and/or overgrowth of a film led to the development of PRS [15], which is discussed below in more detail. The sensitivity chart of BAS is shown in Fig. 5 for typical R_p and φ_B values encountered for semiconductors in the weak to medium absorbent regime in form of iso-R_p and iso-φ_B contours in the $\varepsilon_1 - \varepsilon_2$ plane. The complete solution is given in Ref. [27].

Each of the above reflectance-based characterization technique has an valid range of applications fitting the needs of characterization accuracy. Even though Ellipsometry has been perfected and established during the last 30 years as an important diagnostic tool for material and thin film characterization, the need of either simplicity or higher sensitivity drives the development of reflectance-based characterization techniques that improve or supplement present techniques.

3. Thin film characterization

The demand of optical thin film characterization can be divided in at least two sections:

- obtaining the optical properties of a thin film or stack of films after the growth process, and
- the real-time monitoring and characterization of film growth.

For the post-growth analysis, whether applied in-situ or ex-situ, a variety of macroscopic and microscopic analysis techniques, such as Spectroscopic Ellipsometry (SE), spectroscopic and/or polarization modulated reflectance techniques, near-field optical spectroscopy, or Raman Spectroscopy, are available, which-combined with structural techniques such as XRD, TEM, SIMS-can be used to retrieve the film properties. All reflectance-based optical techniques are discussed in Section 2 can also be applied to thin film characterization.

However, the real-time film characterization is the more challenging part, since real-time characterization techniques underlay additional constrains, such as

1. non-interference with the growth process,
2. withstanding hostile growth environments,
3. restrictions in access paths to the substrate/growth surface,
4. robustness and simplicity in setup, alignment and operation,
5. the time available for one measurement point before a growth parameter has been changed, and
6. very crucial, the sensitivity of the probe technique to film formation and surface processes.

The advantages of using real-time optical characterization techniques are manifold. The in real-time gathered optical response from a growth surface can be either directly linked to control a growth process (see closed-loop feed-back control) to control composition and/or thickness of a (multi-) layer stack, or it can simply be recorded and analyzed after the growth integrating additional compositional and structural film data obtained by post-growth characterization techniques. The non-destructive character of an optical probe beam employed onto a growth surface, allows its implementation in most commonly used low-pressure deposition processes. Some restrictions are experienced in plasma-processes where interactions of the probe beam with excited species in the ambient can be expected. Even though real-time optical characterization provide a vast amount of information, the challenge is how to correlate the observed features to relevant growth parameter and growth optimization.

3.1. Reflectance methods for multi-media

For complementary descriptions of optical diagnostics for thin films, we refer to Heavens [37], Azzam et al., [20], Herman [21], and Bauer and Richter [22]. In the following description provided, we will maintain the notation for propagation of electromagnetic waves, introduced in Section 1.2, and give all expressions formulated in MKSA units. For the complex values we use two formulations synonym:

$$\text{complex dielectric function } \varepsilon = \varepsilon^{r} - i\ \varepsilon^{i} = Re(\varepsilon) + \mathrm{Im}(\varepsilon_r, \varepsilon_i).$$

Fresnel's equations for a multi-layer stack, as schematically shown in Fig. 6, are used to calculate the changes of the reflectivity for s- or p-polarized light as a function of layer thickness, assuming homogenous isotropic media. Numbering the media forming the multi-layer stack through, starting with '0' for ambient, the reflectance coefficients $r_{k(k+1)}$ for the interfaces are given in Ref. [37]

$$r_p|_{k(k+1)} = \frac{\varepsilon_{k+1}\sqrt{\varepsilon_k - \varepsilon_0 \sin^2\varphi} - \varepsilon_k\sqrt{\varepsilon_{k+1} - \varepsilon_0 \sin^2\varphi}}{\varepsilon_{k+1}\sqrt{\varepsilon_k - \varepsilon_0 \sin^2\varphi} + \varepsilon_k\sqrt{\varepsilon_{k+1} - \varepsilon_0 \sin^2\varphi}} \quad (k \geq 0). \tag{3.1}$$

and

$$r_s|_{k(k+1)} = \frac{\sqrt{\varepsilon_k}\cos\varphi - \sqrt{\varepsilon_{k+1} - \varepsilon_0 \sin^2\varphi}}{\sqrt{\varepsilon_k}\cos\varphi + \sqrt{\varepsilon_{k+1} - \varepsilon_0 \sin^2\varphi}} \quad (k \geq 0). \tag{3.2}$$

To determine the total reflected beam and phase change from such a multi-layered medium, we have to sum over amplitudes of the successive beams reflected and transmitted on each interface building up the layered stack. The principle solution was first presented by Airy [38] performed for a single transparent film. More generalized comprehensive descriptions are given by Heavens [37] and Azzam [20]. The change in the phase of the beam traversing through the kth layer is given by

$$\Phi_k = \frac{2\pi d_k}{\lambda}\sqrt{\varepsilon_k - \varepsilon_0 \sin^2\varphi} \quad (k \geq 1). \tag{3.3}$$

where λ denotes the wavelength and d_k and ε_k the thickness and the complex dielectric function of the kth layer. The summation of all amplitudes reflected and transmitted on the interfaces contributing to the total reflected amplitude rr_n can be calculated from a 'k'-2 × 2 matrix multiplication

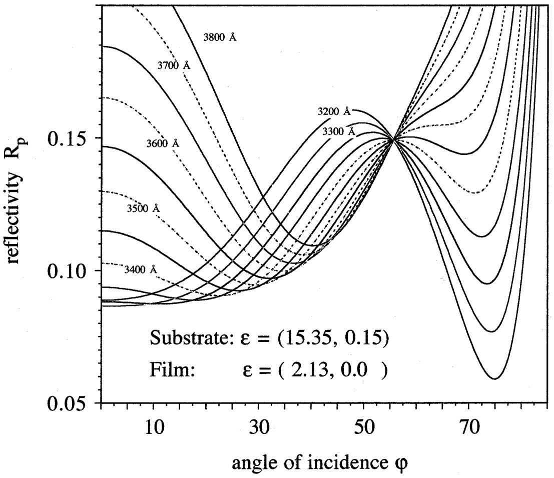

Fig. 7. Angle dependent evolution of reflectivity R_p during film growth, using SiO_2 on Si ($\lambda = 632$ nm) as an example. The angle at which the reflectivity stays constant is the pseudo-Brewster angle of the film.

$$\begin{bmatrix} M_{11} & M_{12} \\ M_{21} & M_{22} \end{bmatrix} = \begin{bmatrix} 1 & r_{01} \\ r_{01} & 1 \end{bmatrix} \times \begin{bmatrix} 1 & r_{12} \\ r_{12}\,e^{-2i\Phi_k} & e^{-2i\Phi_1} \end{bmatrix} \times \begin{bmatrix} 1 & r_{23} \\ r_{23}\,e^{-2j\Phi_2} & e^{-2i\Phi_2} \end{bmatrix} \cdots \times \begin{bmatrix} 1 & r_{(k-1)k} \\ r_{(k-1)k}\,e^{-2i\Phi_k} & e^{-2i\Phi_k} \end{bmatrix}, \tag{3.4}$$

with the reflectance amplitude of p-polarized light given by

$$rr_k = \frac{M_{21}}{M_{11}}. \tag{3.5}$$

For a single layer, the reflected amplitude rr_k reduces to

$$rr_1 = \frac{M_{21}}{M_{11}} = \frac{r_{01} + r_{12}\,e^{-2i\Phi_1}}{1 + r_{01}r_{12}\,e^{-2i\Phi_1}}, \tag{3.6}$$

and the reflectivity $R = rr_1 \times rr_1^*$.

The description above can be apply for any reflectance-based optical characterization technique to analyze layer thickness and optical film properties. The difficulty, however, is the inversion of the equation to obtain an analytical functional relationship $\varepsilon = f\{R(d_1,\varepsilon_1,\ldots,d_k,\varepsilon_k)\}$. Various approximations have been presented to obtain such linkages for different experimental conditions.

To invert the fundamental equations for ellipsometry for a three-phase system computational methods and various approximations [39,40] are well documented in the literature.

3.2. Brewster angle reflectance techniques for thin film characterization

Using the highly sensitive Brewster angle condition to determine the optical properties of thin films has a long tradition. In 1949, Abeles [41] devised a method for the determination of refractive index of a transparent film, by comparing the angle dependent reflectivity values of an uncoated substrate with that of a transparent coated film. The phenomena is demonstrated in Fig. 7, which shows the angle dependent changes in the reflectivity R_p for various film thicknesses in the range of 3200–3800 Å, assuming the optical properties of a SiO_2 film to top of a Si substrate monitored at $\lambda = 632.8$ nm. The angle of incidence at which the reflectance is constant is $\varphi = 55.58°$. Using Eq. (2.12), we obtain for the film a refractive index of $n = 1.459$. Kelly and Heavens [42] introduced an experimental setup that applying this method to obtain the refractive index of a transparent film on a metal surface. The same effect has been described by Jungk [43], who proposed an experiment setup to determined the optical constant of a SiO_2 layers on Si. In order to simplify the expression for the reflectance as a function of surface layer overlayer and

ε_p, McIntyre and Aspnes [39,40] discussed theoretically the change in the reflectance, $\Delta R/R = (R_{afs} - R_{as})/R_{as}$, for thin surface layer (thickness $d_p \ll \lambda$) using a linear approximation in the phase factor Φ_f for a three layer (ambient/film/substrate) stack.

In 1973, A. Balzarotti et al. [44] proposed a method that analyzes the derivative $dR_p/d\varphi$ around the pseudo-Brewster angle φ_B and presented approximated analytical expressions for weak absorbent media. He also pointed out the high sensitivity of his technique towards surface modifications and discussed the potential use of this technique to characterize surface layers.

The application towards determination of thickness of organic layers on solid substrates has been described by Arwin et al. [45,46].

However, the complexity of angle dependent Fresnel's equations made it almost impossible to formulate general analytical expressions that link the optical materials properties to the measurement values, which restricted their use to special experimental application. Progress in the formulation of analytical relations was made by Azzam et al., [35,54] and by the readiness availability of computing power, which allowed the numerical analysis of the expressions. End of the 80th, Kobayashi et al. [13,47–51] utilized the sensitivity of p-polarized light in the vicinity near the Brewster angle towards real-time monitoring of surface chemical composition during epitaxial GaAs growth using metalorganic precursor. Their application focused on the strong absorbing region of a compound semiconductor in order to gain high sensitivity towards surface processes. The technique was denoted accordingly as SPA. The theoretical interpretation of the SPA signal has been described by Horikoshi et al. [52] and Hingerl et al. [53], who calculated the changes in $\Delta R/R$ under SPA conditions and provided the basis for detecting process-induced changes in surface chemical composition by photo-absorption (SPA).

The concept of PRS was introduced through [17] and is based on the spectroscopic analysis of differences in the dielectric functions of different media. Both, SPA and PRS, are utilizing the p-polarized light near the pseudo-Brewster angle of a medium to suppress the bulk reflectance component in favor to (near-) surface contributions. In contrast to SPA, which restricts itself to the highly absorbent wavelength region, PRS is applied in the transparent and weak absorbent wavelength range in order to analyze differences in the dielectric functions of different media. As shown in Section 3.1, each interface between two media gives rise to a complex reflectance coefficient and a with it contributes to the total reflected intensity. In a heterostructural film growth process we have to consider a minimum of two interfaces: (a) ambient ($\varepsilon_a = 1$) and film ($\varepsilon_f > 1$), and (b) film ($\varepsilon_f > 1$) and substrate ($\varepsilon_s > 1$). Depending on the complexity of a heterostructure stack, the number of interfaces contributing to the reflected intensity can become quite large, making it increasing difficult to separate the various contributions. A further complication arises from the fact that not only the differences in the dielectric functions, but also the interface perfection enter as a parameter in reflectance coefficient for each interface.

The pseudo-Brewster angle law for an ideal interface can be formulated as a function of the complex optical functions ε. As shown in Section 1.2, the influence of the absorbing media on the Brewster angle can be expressed as a shift in the angle φ_B at which and in an offset, i.e. $R_p|_{\varphi_B} \geq 0$. For weakly absorbing media, the reflectivity $R_p|_{\varphi_B}$ lies in the order of 10^{-6}–10^{-4} and increases up to 10^{-2} for strong absorbing media, such as metals. Assuming the growth of an ideal two-dimensional layer and a given dielectric function ε of a substrate, the reflected light from the surface can be initially split in two contributions. One contribution related to the bulk properties of the substrate and second contribution due to the growing film. For an angle of incidence near the Brewster angle φ_B of the substrate, the bulk contribution strongly suppressed allowing highly sensitive detection of heterostructural film nucleation and overgrowth processes. With this, a high surface sensitivity. The PRS configuration by choice of an appropriate probe wavelength, information from Since. The richness of information obtained in such a real-time growth monitoring is demonstrate in Section 3.3.

Further, changes in the growth conditions, such as a variation in the growth rate, density fluctuations or changes in the optical function ε during the growth results in a change of the slope in the monitored reflectance spectrum or in a discontinuity in the derivative reflectance spectrum, respectively.

3.3. Thin film growth characterization by p-polarized reflectance spectroscopy

Applying optical probe techniques towards real-time characterization of thin film growth, involving metalorganic precursors, inherits the challenge to relate surface chemistry processes that drives the growth process, towards growth/film properties, such as composition, instantaneous growth rate or structural layer quality. Characterization and understanding of surface chemistry processes requires the development of high sensitive methods to characterize growth, ideally at the point where the growth process itself occurs and might be controllable. Many of the present efforts are directed towards accurately measuring ambient process parameters, such as pressure, flux or temperature, since numerous probes are available to provide a relative detailed assessment of the ambient. However, this strategy is clearly limited in its capability to deal with complex

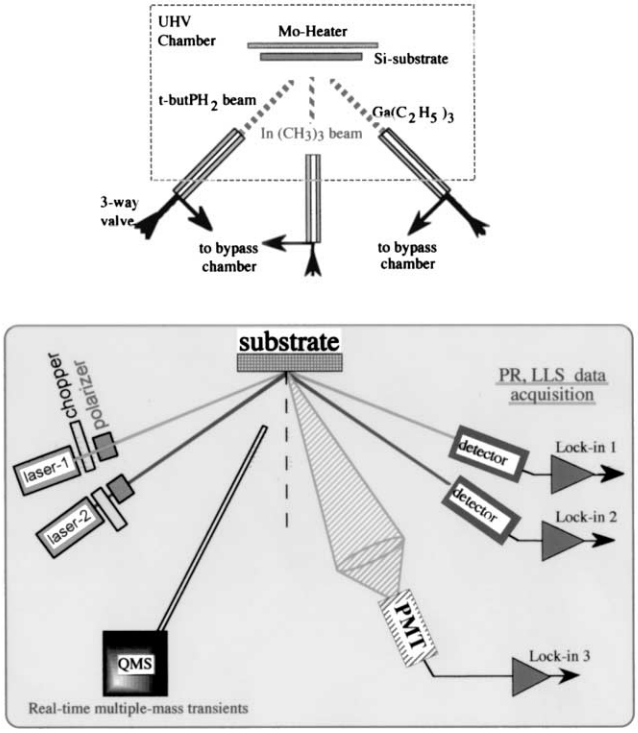

Fig. 8. Schematic illustration of: (a) PCBE setup; and (b) PRS- and LLS-setup.

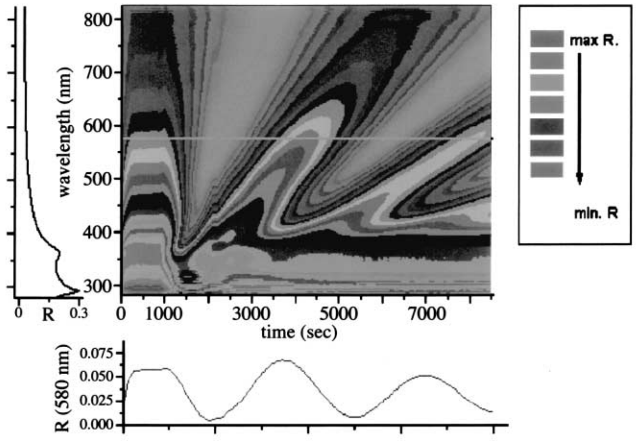

Fig. 9. Iso-plot of the PRS evolution for heteroepitaxial GaP growth on Si under PCBE conditions at 450 °C, monitored at an angle of incidence of 70° from 280 to 850 nm with a resolution of 200 ms per spectrum.

nonlinear surface chemistry processes, where the surface plays an integral role in the precursor decomposition pathways and small changes in the ambient composition can affect the growth substantially.

PRS is a p-polarized reflectance technique that achieves enhanced surface sensitivity through the fact that the bulk reflectance vanishes when p-polarized light is incident on transparent or weak absorbent material at the pseudo-Brewster angle. This configuration allows to monitor changes at the surface or near-surface processes, making PRS suitable to follow surface modification as they occur for example during heteroepitaxial nucleation and overgrowth period of the substrate or during periodic change in the surface chemistry during pulsed precursor exposure. To illustrate the sensitivity of PRS we show in the following results obtained during single-wavelength PRS real-time monitoring of the heteroepitaxial growth of GaP on Si(001). For this work pulsed chemical beam epitaxy (PCBE) is used, that is, the surface of the substrate is exposed to pulsed ballistic beams of *tertiary*-butylphosphine (TBP), tri-ethyl-gallium (TEG) and activated hydrogen at typically 350 °C to accomplish nucleation and overgrowth of the Si by an epitaxial GaP film. The fluxes of TEG [$Ga(C_2H_5)_3$], TBP [$(C_4H_9)PH_2$] and hydrogen, are established by mass flow controllers and are directed via computer-controlled three-way valves to either the reactor chamber or a separately pumped bypass. This allows the sequential exposure of the substrate to individual pulses of the precursor molecules. The switching of the sources is synchronized with the data acquisition of the PRS and LLS signals to correlate changes in the reflected light intensity with the changes in the optical properties of the heteroepitaxial stack and with changes in the thickness and optical properties of the epitaxial film.

Utilizing the high sensitivity of a Brewster angle condition, we introduced PRS as an optical probe technique for both, surface- and thin film characterization technique. Its sensitivity and capability has been demonstrated during PCBE of III–V heteroepitaxial growth. The demonstrated high sensitivity of PRS to surface reaction processes in the context of real-time monitoring of PCBE has opened new possibilities for characterization and control of thin film deposition processes.

The PRS sensors are integrated in the PCBE system as schematically shown in Fig. 8(a). In PCBE, the surface of the substrate is exposed to pulsed ballistic beams of TBP [$(C_4H_9)PH_2$] and TEG [$Ga(C_2H_5)_3$] and TMI [$In(CH_3)_3$] at typically 350–450 °C to accomplish nucleation and overgrowth of the silicon by an epitaxial $GaP/Ga_{1-x}In_xP$ film. For PRS and LLS p-polarized light beams ($\lambda_1 = 632.8$ nm, $\lambda_2 = 700$ nm or Xe-lamp) are employed using Glan-Thompson prisms, as illustrated in Fig. 8(b). The beams impinge on the substrate at an angle of incidence of $\varphi = 70$ and 75°, respectively. Further details on the experimental conditions are given in the previous publications [16,17,55–66].

Fig. 9 shows an iso-plot of the evolution of the PRS spectrum during growth of GaP on Si(001) at 420 °C, recorded at an angle of incidence of $\varphi = 71°$. During growth, each 200 ms a complete spectrum in the wavelength range from 280 to 850 nm is recorded. The inset on the left side shows the reflectivity of the Si substrate before the growth has been initiated. The lower graph

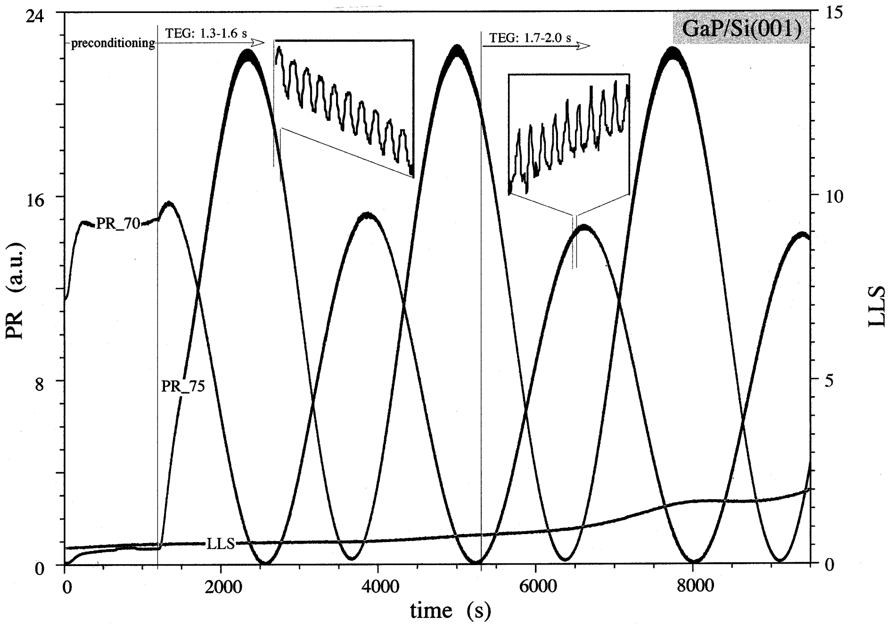

Fig. 10. Temporal evolution of PR signals monitored at two wavelengths at two angles of incidence during heteroepitaxial GaP growth under PCBE growth conditions.

shows the temporal evolution of the reflectivity at a selective wavelength ($\lambda = 580$ nm) during the growth process. The vast amount of data is strongly compressed and only the overall evolution is shown.

Fig. 10 shows in more detail the single-wavelength PR and LLS signals during heteroepitaxial growth of GaP on Si(001). After initiating growth at 1200 s, minima and maxima are observed in the time evolution of the PR signals due to the interference phenomena as the film grows. Please note that both signals are phase shifted, which is due to the fact that one angle of incidence (PR75) is above and the other (PR70) below the pseudo-Brewster angle of the growing film. Superimposed on the interference oscillations of the reflected intensity is a fine structure that is strongly correlated to the time sequence of the supply of precursors employed during the steady-state growth conditions. The two insets in Fig. 10 show enlarged the fine structure evolutions for 30 s of growth for PR75 and PR70, respectively. The fine structure observed in the PR signal is strongly correlated to the time sequence of the supply of precursors employed during the steady-state growth of GaP. Each peak in the fine structure corresponds to a complete precursor cycle with the start of the oscillation coinciding with the leading edge of the first TBP pulse of the sequence.

As seen in Fig. 10, the amplitude in the fine structure undergoes periodic changes during deposition time. The amplitude increases on the raising flank of the interference oscillation with a maximum at the top, and then decreases on the falling flank. The relative locations of these decreases and increases in the fine structure amplitude and the film interference oscillation strongly depend on the chosen growth conditions, such as precursor pulse width and height, pulse sequence time, or supply of additional activated hydrogen. The correlation of the fine structure evolution with the pulsing sequence of the precursor supply is shown in more detail in Fig. 11. The PR response is taken during steady-state growth on a rising flank of an interference fringe using a pulse cycle sequence of 3 s, a TBP pulse form 0.0 to 0.8 s, a TEG pulse from 1.3 to 1.6 s and continuous hydrogen flow during the complete sequence (Table 1).

Analyzing the amplitude evolution of the fine structure superimposed on the PR interference fringes reveals two important features:

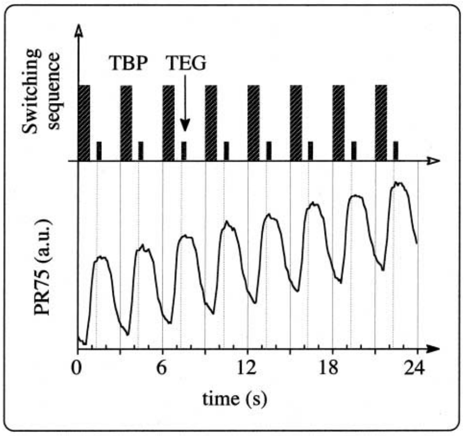

Fig. 11. PR75 response to periodic exposure of growth surface to TBP and TEG precursor pulses, taken at the rising flank of an interference fringe. The total cycle time is 3 s with TPB pulses from 0 to 0.8 s and TEG pulses from 1.3 to 1.6 s.

Table 1
Characteristic features in the PRS and LLS signals and related information

Observed feature	Related information
Changes in the reflected intensity during heat-up	Temperature dependence of the dielectric function of the substrate and surface conditioning
Spacing in the minima/maxima of the film interference oscillation	Growth rate
Amplitude of film interference oscillation	Dielectric function of film in relation to substrate
Excess structure in the PR signal during the initial nucleation period	Growth mechanism
Fine structure oscillations	Surface chemistry and kinetics
Locations of turning points of the fine structure with respect to the minima/maxima of the interference oscillations	Imaginary part of the dielectric function of the surface reaction layer
Bimodal envelope modulation of the fine structure	Surface reconstruction
Evolution of scattered light	Surface roughening/interface perfection/defect formation

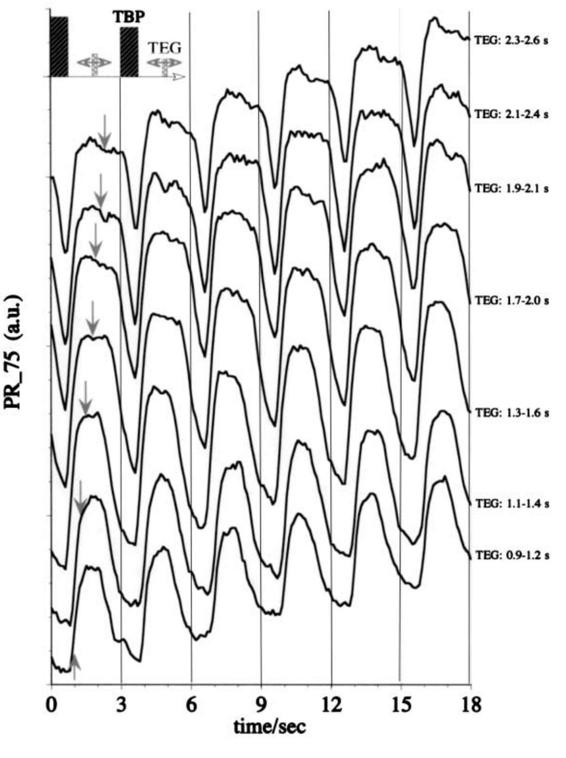

Fig. 12. PR75 responses for various TEG positions within a cycle sequence. The TBP exposure time, position and flux were kept constant. The flux and surface exposure time to TEG were constant; only the start point (marked by an arrow) was changed. The TEG start positions were changed in steps of 0.2 s from (1) 0.9–1.2 s up to (8) 2.3–2.6 s.

1. A periodic increase and decrease in the amplitude of the fine structure that is tagged to the interference oscillations. The relative positions of minima in the fine structure amplitude with respect to the positions in the minima of the interference oscillations depend strongly on the chosen process conditions.
2. A change of the signs of the response to the TBP and TEG pulses at the minima in the fine structure amplitude is observed. The (time) positions of these turn-over points in the pulse response will be denoted as turning points in the PR fine structure in the further text.

The correlation of the fine structure evolution with surface reaction kinetics processes has been studied during pulsed precursor supply as shown in Fig. 12. This figure composed a series of experiments, where the position of the TEG pulse—within a fixed TEG/TBP cycle—is varied as indicated by the arrows in Fig. 12. For comparison, all PR responses are taken at the same intensity/reflectance level on a rising flank of an interference oscillation. The PR response is recorded during steady-state growth using a pulse cycle sequence of 3 s, a TBP pulse from 0.0 to 0.8 s, a TEG pulse of 300 ms duration and continuous hydrogen flow during the complete sequence. To relate the PR information to changes in surface reaction kinetics, the exposure times as well as the precursor fluxes are identical for each trace shown in Fig. 12. An analysis and discussion of these results are presented in Section 3.5.

For heteroepitaxial $Ga_{1-x}In_xP$ growth under PCBE conditions, two different precursor cycle sequences were be explored. The first approach uses the same cycle sequence as for GaP growth with simultaneous injection of TEG and TMI. The second approach uses a sequential injection of TEG and TMI pulses as schematically shown in Fig. 13. Here, the total precursor cycle sequence is expanded in time (equals to two GaP precursor cycle sequences) and each III-precursor (TEG or TMI) is followed by TBP pulse. In this pulsing configuration the optical response to each exposure can be analyzed individually and compared to each other.

Fig. 14 shows the evolution of the PR signals during growth of $Ga_{1-x}In_xP$/GaP on Si(001) at 420 °C,

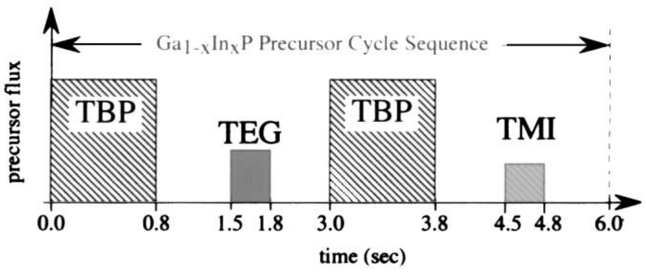

Fig. 13. Schematic representation of a precursor cycle sequence used for the growth of the ternary compound semiconductor $Ga_{1-x}In_xP$ grown via the organometallic precursors TBP, TEG and TMI.

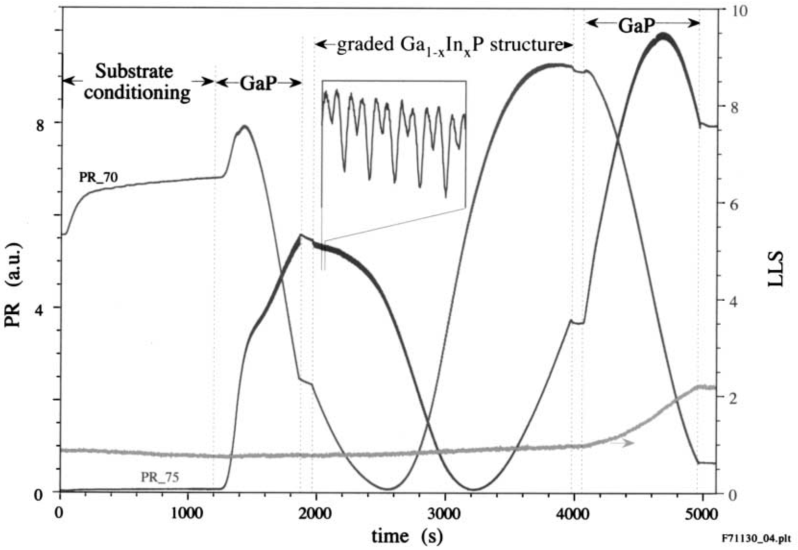

Fig. 14. Growth monitored by PRS during heteroepitasial $Ga_{1-x}IN_xP$/GaP on Si(001).

recorded for PR70 (angle of incidence 71°) and PR75(angle of incidence 75.1°) at $\lambda = 650 \pm 5$ nm and at $\lambda = 632.8$ nm, respectively. The growth process is composed in four sections: (a) substrate and surface preconditioning; (b) deposition of a GaP buffer layer; (c) growth of a compositional graded $Ga_{1-x}In_xP$ layer, and (d) growth of a GaP cap layer. Note that both PR signals are phase shifted, which is due to the fact that one angle of incidence (PR75) is above- and the other (PR70) below-the pseudo-Brewster angle of the growing film material. Superimposed on the PR interference fringes is a fine structure (see inset in Fig. 14) that is strongly correlated to the time sequence of the supply of precursors employed during the steady-state growth conditions.

The compositional graded $Ga_{1-x}In_xP$ layer region is shown in more detail in Fig. 15, together via the estimation of composition as determined by X-ray diffraction analysis. The insets show the variation in the fine structure of the PR signals as response to the different precursor fluxes of TEG and TMI. A correlation of fine structure evolution with the precursor pulsing sequence for different TMI:TEG ratio is shown in Fig. 16. The PR responses are taken from several different growth experiments on the increasing flank of on PR_70 interference fringe. The increase in slope with increasing TMI:TEG ratio correlates to increase in growth rate, while the change in the fine structure response to the individual precursor pulse relates to the change in molar concentrations of constituents in the SRL. Note, the PR fine structure response with approximate same amount of TMI and TEG (TMI:TEG ratio = 1) does not results in the same PR amplitude after TMI and TEG exposure, since the optical response factors for different surface constituents and their molar concentration vary.

3.4. PRS model considerations

For monochromatic light which is parallel polarized to the plane of incidence, no perpendicular reflectance components, r_s, have to be considered as, only the parallel reflectance components, r_p, contribute to the reflectance amplitude. For brevity, the index p will be dropped in the following text. Taking in account a SRL on top of the growing film, Fresnel's equations for at least a four media stack, as schematically shown in Fig. 17, has to be used to calculate the changes of the reflectivity for p-polarized light as a function of layer thickness, assuming homogenous isotropic media.

Numbering the four layer media, '0' denotes the ambient, '1' the SRL, '2' the film, and '3' the substrate,

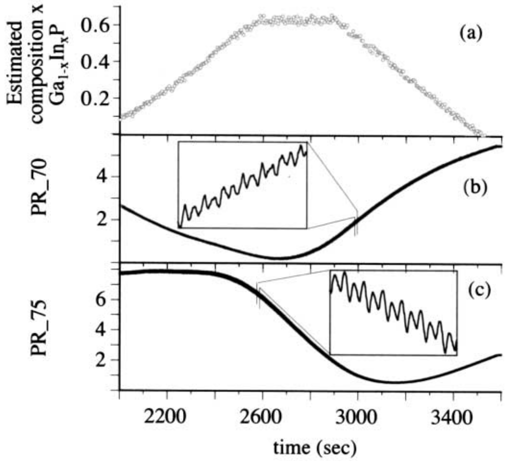

Fig. 15. Growth of a compositional graded $Ga_{1-x}In_xP$ layer (see regions marked in Fig. 14). (a) Estimated composition, determined via ex-situ X-ray diffraction analysis. (b) and (c) evolution of the PR signals. The insets show the fine structure response at two different positions with different TMI:TEG flow-ratios and different PR responses to it.

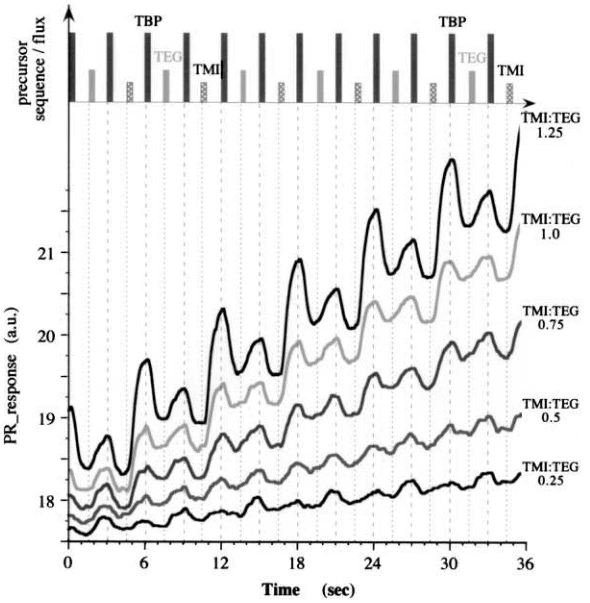

Fig. 16. PR70 responses as function of TMI:TEG ratio during GaInP growth.

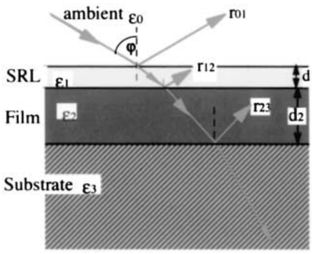

Fig. 17. Schematic representation of a four layer media

with their complex dielectric constants ε_0, ε_1, ε_2 and ε_3, respectively. The reflectance coefficients $r_{k(k+1)}$ for the interfaces are given by Eq. (3.1) and the complex reflectance amplitude rr_4 for p-polarized light is given by Eq. (3.6)

$$rr_4 = \frac{r_{01} + r_{12}\,\mathrm{e}^{-2\mathrm{j}\Phi_1} + r_{23}\,\mathrm{e}^{-2\mathrm{j}(\Phi_1+\Phi_2)} + r_{01}r_{12}r_{23}\,\mathrm{e}^{-2\mathrm{j}\Phi_2}}{1 + r_{01}r_{12}\,\mathrm{e}^{-2\mathrm{j}\Phi_1} + r_{01}r_{23}\,\mathrm{e}^{-2\mathrm{j}(\Phi_1+\Phi_2)} + r_{12}r_{23}\,\mathrm{e}^{-2\mathrm{j}\Phi_2}}, \tag{3.7}$$

with the two phase factors

$$\Phi_1(t) = \frac{2\pi\hat{d}_1(t)}{\lambda}\sqrt{\hat{\varepsilon}_1(t) - \varepsilon_0\sin^2\varphi}, \tag{3.8}$$

and

$$\Phi_2(t) = \frac{2\pi d_2(t)}{\lambda}\sqrt{\varepsilon_2 - \varepsilon_0\sin^2\varphi}. \tag{3.9}$$

$d_1(t)$ and $d_2(t)$are the thicknesses of SRL and film, respectively, λ is the wavelength of the reflected p-polarized laser beam and φ the angle of incidence.

The four media reflectivity, given by $R_4 = rr_4{}^{\bullet}rr_4^*$, can be approximated in a linear expansion for rr_4 in Φ_1 by

$$rr_4 \approx rr_4(\Phi_1 = 0) + \Phi\frac{\partial rr4}{\partial\Phi_1}\bigg|_{\Phi_1=0} = rr_3 + rr_{4\alpha}\Phi_1, \tag{3.10}$$

With this, the reflectivity can be written as

$$\begin{aligned} R_4\big|_{\mathrm{ap}} &\approx rr_3rr_3^* + rr_3\Phi_1^*rr_{4\alpha}^* + rr_3^*\Phi_1rr_{4\alpha} + |\Phi_1|^2|rr_{4\alpha}|^2 \\ &= R_3 + 2\mathrm{Re}\{rr_3^*\Phi_1rr_{4\alpha}\} + |\Phi_1|^2|rr_{4\alpha}|^2 \\ &= R_3 + \Delta R_{4-3}. \end{aligned} \tag{3.11}$$

where R_3 denotes the reflectivity for the three-layer stack (without SRL), $\mathit{\Delta} R_{4-3}$ the linear approximation of the SRL contribution and $rr_{4\alpha}$ the derivative of the complex reflectance amplitude rr_4 in Φ_1 at $\Phi_1 = 0$.

The first derivative of rr_4 in Φ_1 is given by the expression

$$\frac{\partial rr_4}{\partial\Phi_1} = \frac{-2\mathrm{j}\,\mathrm{e}^{-2\mathrm{j}\Phi_1}(1 - r_{01}^2)(r_{12} + r_{23}\,\mathrm{e}^{-2\mathrm{j}\Phi_2})(1 + r_{12}r_{23}\,\mathrm{e}^{-2\mathrm{j}\Phi_2})}{(1 + r_{01}r_{12}\,\mathrm{e}^{-2\mathrm{j}\Phi_1})^2 + 2\xi_1r_{23}\,\mathrm{e}^{-2\mathrm{j}\Phi_2} + r_{23}^2(r_{12}r_{01}\,\mathrm{e}^{-2\mathrm{j}\Phi_1})^2\,\mathrm{e}^{-4\mathrm{j}\Phi_2}}, \tag{3.12}$$

with

$$\xi_1 = r_{12}r_{01}\,\mathrm{e}^{-2\mathrm{j}\Phi_1}(1 + r_{12}^2 + r_{01}r_{12}\,\mathrm{e}^{-2\mathrm{j}\Phi_1}).$$

In the analysis of the timely evolution of the fine structure which is superimposed with the interference

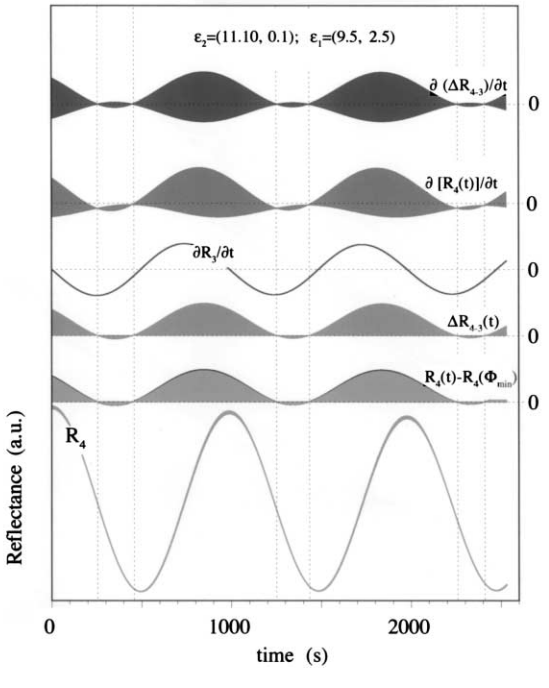

Fig. 18. Simulated temporal evolution of the PR signal monitored at $\varphi = 72°$, $\lambda = 632.8$ nm for a four layer media model. The dashed lines mark the positions of the turning points. Also shown are the first derivatives of the PR signal and contributions related to the SRL (see text). With $\varepsilon_1(\lambda = 632.8\ \text{nm}) = (9.5,\ 2.5)$ a minimal thickness of $d_{1\min} = 0.5$ Å ($\rightarrow \phi_{1\min}$) and maximal thickness of $d_{1\max} = 5$ Å ($\rightarrow \phi_{1\max}$), and an ambient with $\varepsilon_0 = 1$.

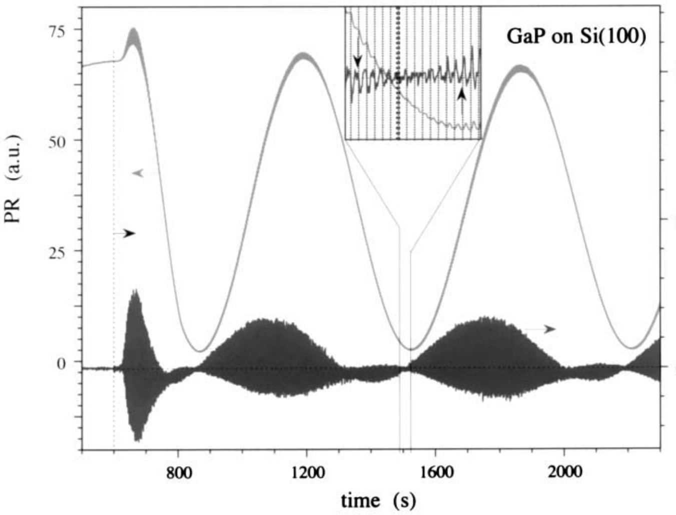

Fig. 19. PR signal monitored at an angle of incidence of 70° using a HeNe laser and d(PR)/dt evolution for heteroepitaxial GaP growth on Si under PCBE conditions at 350 °C. The insert shows an enlargement around a turning point, where the response to the TBP precursor (marked by arrows) changes sign.

oscillations of the underlying growing film, the different time evolutions of the both phase factors Φ_1 and Φ_2 can be utilized to separate contributions related to the SRL and thus related to the bulk film [62]. Fig. 18 shows the simulated reflectivity for a four layer media built up by the substrate Si, the growth of GaP layer with an average deposition rate of 1 Å/s, and a periodic in thickness modulated SRL. For comparison, Fig. 19 shows the evolution of the PRS signal with its first derivative during the growth of GaP on Si(001) at 350 °C with a precursor cycle sequence time of 3 s. The envelope function of d(PR)/dt shows two important features:

1. At the beginning of the heteroepitaxial growth process—after an incubation period of several precursor cycle sequences—a rapid increase in the d(PR)/dt amplitude is observed.
2. After the heteroepitaxial nucleation and overgrowth, the d(PR)/dt evolution undergoes period oscillations, where one oscillation consists of a long period with a large amplitude and a short period with a small amplitude. The ratio of these periods and their amplitude strongly depends on the chosen precursor fluxes and exposure times. The extrema expanded in the inset of Fig. 19 shows the position were a turning point in the fine structure occurs.

The deviation of the envelope function in d(PR)/dt during the first 200 s of heteroepitaxial growth indicates that the nucleation and overgrowth process may extend 60–70 cycle sequences before quasi steady-state growth conditions are reached. This confirms reflectance difference (RD) observations which revealed an increase in the anisotropy during the first 100 s of nucleation and overgrowth [60]. A more detailed analysis and review on real-time characterization of early stages of heteroepitaxial overgrowth is given by Bachmann et al. [67].

3.5. Reduced order surface kinetics (ROSK) model for $Ga_{1-x}In_xP$ deposition

In the case of heteroepitaxial $Ga_xIn_{1-x}P$ growth on Si employing triethylgallium [TEG, $Ga(C_2H_5)_3$], trimethylindium [TMI, $In(CH_3)_3$], and tertiary-butylphosphine [TBP, $(C_4H_9)PH_2$] as source vapors, efficient fragmentation and sufficient retention of fragments on the surface occurs within a limited process window in the temperature range 600 $K \leq T \leq 750$ K for Si(100) [14]. The kinetics of TEG pyrolysis for the growth of GaP on Si(100) utilizing triethylgallium and TBP as source vapors has been discussed in detail elsewhere [63,68,69]. Its progression can be summarized in three consecutive steps:

$$Ga(C_2H_5)_3 \rightarrow Ga(C_2H_2)_2^{\bullet} + C_2H_5^{\bullet}, \tag{3.13}$$

$$Ga(C_2H_5)_2 \rightarrow |GaC_2H_5 + C_2H_5^{\bullet}, \tag{3.14}$$

$$|GaC_2H_5 \rightarrow |Ga^{\bullet} + C_2H_5^{\bullet}, \tag{3.15}$$

where the vertical dashes and superscript dots denote lone electron pairs and single valence electrons, respectively. Similarly, we may describe the decomposition kinetics of TMI pyrolysis for heteroepitaxial growth of utilizing trimethylindium in three consecutive steps [68]. Its progression might be summarized in three consecutive steps:

$$In(CH_3)_3 \rightarrow In(CH_2)_2^{\bullet} + CH_3^{\bullet}, \tag{3.16}$$

$$In(CH_3)_2 \rightarrow |InCH_3 + CH_3^{\bullet}, \tag{3.17}$$

$$|InCH_3 \rightarrow |In^{\bullet} + CH_3^{\bullet}, \tag{3.18}$$

Also, the thermal decomposition of TBP has been studied in detail [70,71] and proceeds through a series of consecutive reactions summarized by

$$(C_4H_9)PH_2 \rightarrow |PH_2^{\bullet} + C_4H_9^{\bullet}, \tag{3.19}$$

$$C_4H_9^{\bullet} + (C_4H_9)PH_2 \rightarrow (C_4H_9)\bar{P}H^{\bullet} + C_4H_{10}, \tag{3.20}$$

$$|C_4H_9|\bar{P}H^{\bullet} \rightarrow |\bar{P}H + C_4H_9^{\bullet}. \tag{3.21}$$

For GaP growth on Si(100), we have shown that the decomposition of TBP is fast and elimination of ethyl radicals from the TEG fragments represents the rate limiting step [72]. In a realistic model, the SRL represents a multi-component mixed phase with a variety of radical reactions that have to be added to the above reactions (3.13)–(3.21) and to the reaction products from the TEG, TMI and TBP decomposition [72].The thickness and composition of the SRL depends on the relative heights and widths of the employed TMI, TEG and TBP source vapor pulses and their repetition rate. We note that some of the intermediate fragments of the source vapor molecules in the SRL that feed the growth process may carry permanent dipole moment, which are likely to contribute to the stabilization of the SRL [63]. In view of intermolecular interactions, deviations of the SRL from ideal behavior can be expected. However, the objective here is to find a 'first approximation model' that allows to relate the measured PR signals to the dynamics of the decomposition processes of the SRL constituents, and to relate the kinetics of growth and real-time modeling for closed-loop process control.

The reduced order kinetic model for the compound semiconductor $Ga_{1-x}In_xP$, summarizes all chemical reactions in one dominant reaction for the TBP pyrolysis (TBP source term: S_{TBP}), two dominant reactions for the TEG decomposition (TEG source term: S_{TEG}), and two dominant reactions for the TMI decomposition process (TMI source term: S_{TMI}). All precursor sources are supplied sequentially separated by pauses as shown schematically in Fig. 13.

Thus the kinetic model representing the SRL reactions is given by the following system of ordinary differential equations for the molar concentrations n_l of SRL constituents:

$$\frac{d}{dt} n_1(t) = n_{TBP} - \tilde{a}_1 n_1(t) - \tilde{a}_4 n_3(t) n_1(t) - \tilde{a}_7 n_6(t) n_1(t), \tag{3.22}$$

$$\frac{d}{dt} n_2(t) = n_{TEG} - \tilde{a}_2 n_2(t), \tag{3.23}$$

$$\frac{d}{dt} n_3(t) = \tilde{a}_2 n_2(t) - \tilde{a}_3 n_3(t) - \tilde{a}_4 n_3(t) n_1(t), \tag{3.24}$$

$$\frac{d}{dt} n_5(t) = n_{TMI} - \tilde{a}_5 n_5(t), \tag{3.25}$$

$$\frac{d}{dt} n_6(t) = \tilde{a}_5 n_5(t) - \tilde{a}_6 n_6(t) - \tilde{a}_7 n_6(t) n_1(t), \tag{3.26}$$

with the two incorporation reactions

$$\frac{d}{dt} n_{GaP}(t) = \tilde{a}_4 n_3(t) n_1(t), \tag{3.27}$$

and

$$\frac{d}{dt} n_{InP}(t) = \tilde{a}_7 n_6(t) n_1(t), \tag{3.28}$$

for GaP and InP, respectively.

(Eqs. (3.22)–(3.24)) describes the reduced order TBP and TEG pyrolysis [66], and Eqs. (3.25) and (3.26) describe the parameterized reduced order TMI pyrolysis. n_{TBP}, n_{TEG} and n_{TMI} denote the periodic supply functions expressed in terms of the molar concentration of TBP-fragments and TEG-fragments reaching the surface. They are linked to the source terms S_{TBP}, S_{TEG} and S_{TMI} via form factors that account for geometrical intercept factors, and for the activation barrier and its temperature dependency. The TEG as well as the TMI pyrolysis is assumed to be described by a two-step decomposition process using two generalized reaction parameters $\tilde{a}_2$, $\tilde{a}_3$, $\tilde{a}_5$ and $\tilde{a}_6$, respectively. The formation of GaP and InP and its incorporation in the underlying film is summarized in the reactions Eqs. (3.27) and (3.28). The composition, x, for the compound semiconductor $Ga_{1-x}In_xP$ is expressed as the averaged ratio of molar concentration over a cycle sequence

$$x = \frac{\int \frac{d}{dt} n_{InP}}{\int \left(\frac{d}{dt} n_{GaP} + \frac{d}{dt} n_{InP} \right)} dt \tag{3.29}$$

and the instant film growth rate g_{fl} is given by

$$g_{fl} = \frac{1}{A}\left[\tilde{V}_{GaP} \frac{d}{dt} n_{GaP} + \tilde{V}_{InP} \frac{d}{dt} n_{InP} \right], \tag{3.30}$$

At this point, the SRL is treated as a homogeneous ideal solution and the surface area, A, is assumed to be constant for simplicity. Also note that the surface structure, number of reaction sides, and inhomogeneous reactions are not explicitly addressed at this point and are integrated into the reaction parameters $\tilde{a}_4$ and $\tilde{a}_7$.

The temporal thickness evolution of the SRL is given by

$$d_1(t) = \frac{1}{A}\,[n_1 \bar{V}_1 + n_2 \bar{V}_2 + n_3 \bar{V}_3 + n_5 \bar{V}_5 + n_6 \bar{V}_6], \tag{3.31}$$

where $\bar{V}_i$ are the molar volumes of the constituents in the SRL.

Based on the above reaction chemistry, we model the linkage between the measured PR signals and the surface kinetics on the basis of a reduced order surface kinetics model and a four-media stack: ambient/SRL/epilayer/substrate, which represents the simplest possible description of the optical response under the conditions of PCBE processes. For the interpretation of the time-dependence of the four media stack reflectance, $R_4(t)$, in terms of the chemical kinetics in the SRL that drives epitaxial growth, the dielectric function of the SRL, ε_1, must be linked to its composition. Such a linkage can be established by approximating the dielectric function of the SRL through an effective dielectric function ε_1, parameterized and expressed as the sum over all molar fractions x_i contributing to the SRL:

$$\varepsilon_i(\omega) = \varepsilon_\infty + \sum_{i \neq 4,7} x_i(t) F_i(\omega) \quad \text{and} \quad x_i(t) = \frac{n_i(t)}{\sum_k n_k(t)}. \tag{3.32}$$

The dielectric function of the SRL is obtained by summing over the contributions of all its constituents, identified by the label *i*. $F_i(\omega)$ in Eq. (3.32) denotes the oscillator strength of the transitions and ω denotes the frequency at which ε_1 is evaluated.

The surface reaction kinetics can be studied by analyzing data as presented in Fig. 12. These data were used to establish an initial data base for modeling of the surface reaction kinetics for heteroepitaxial GaP growth on Si under pulsed CBE conditions with sequential exposure of growth surface to pulses of TBP and TEG as shown in Fig. 20. The figure summarizes results obtained by solving the coupled differential (Eqs. (3.22)–(3.28)), calculating the molar concentrations of the surface constituents, their effective surface layer thickness and the dielectric optical properties and comparing the results with the temporal evolution of the PR response for different precursor fluxes and cycle sequences.

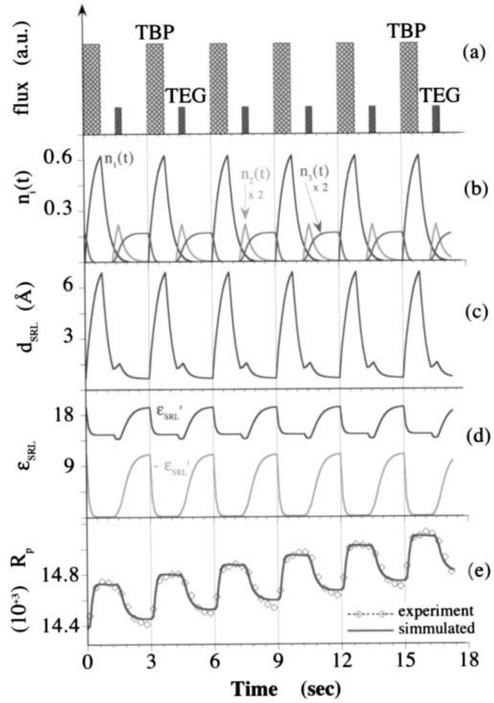

Fig. 20. Modeling of surface reaction kinetics for heteroepitaxial GaP growth on Si under pulsed chemical beam epitaxy conditions with sequential exposure of growth surface to pulses of TBP and TEG. The molar concentrations of the surface constituents, their effective surface layer thickness and the dielectric optical properties are computed using (Eqs. (3.22)–(3.32)). The simulated PR response for $\varphi = 75.1°$ and $\lambda = 632.8$ nm is compared with experimental results.

Since for most growth processes of the relevant, the reactions pathways and their rate constants are presently not known, the establishment of a more detailed surface kinetics model and validating data by relating real-time optical and mass spectroscopic signals to a surface reactions kinetics model has several challenges:

1. most optical techniques observe signals that are related to a macroscopic description of growth with a time-scale of 10^{-3}–10^{-6} s, while a molecular-dynamic models of growth are a time-scale of 10^{-12}–10^{-14} s;
2. relevant decomposition pathways, their rate constants and temperature dependence are not known or are under dispute and
3. to follow the defragmentation of the precursors, surface-sensitive techniques either in the UV or in the IR wavelength range are required. However, in the IR region the infra-red absorption strength of metalalkyls source compounds and their defragmentation products are two to three orders of magnitude lower than in the visible wavelength range, which requires:
   - ○ high-intense light sources,
   - ○ special requirements on detectors and phase sensitive detection electronic (Lock-in),
   - ○ reducing infrared radiation from a hot substrate surface (tunable notch filters) and
   - ○ suppressing substrate reflectance component (for instance Brewster angle condition).

However, the above ROSK model provides a description as how to relate changes in composition and thickness of the SRL to an effective dielectric function $\varepsilon_1(\omega,t)$ and, $d_1(t)$, respectively. With this, the instantaneous composition, *x*, and growth rate $g_{fl}(t)$ for the growth of $Ga_xIn_{1-x}P$ heterostructures under closed-loop feedback, as demonstrated in Section 3.6. For thin film growth control, a data base for the parameter estimation for $Ga_{1-x}In_xP$ growth has to be established and fast filtering and feedback algorithms have to be developed to close the real-time feedback-loop. Even though some of the parameters involved, such as the molar volumes and optical oscillator strengths can be estimated, a larger set of experimental data are required to validate the analysis of surface reaction kinetics.

3.6. Thin film growth control by PRS

The ROSK data are incorporated in Fresnel's equation that determines the reflectance amplitude, *rr*, of the p-polarized light as follows. Consider the four layer

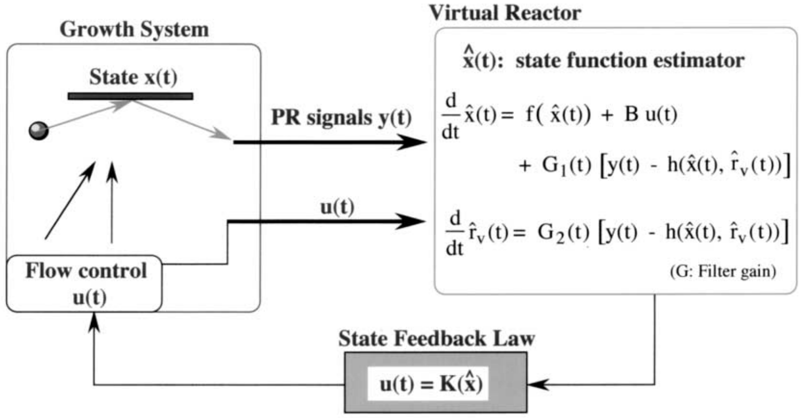

Fig. 21. Control of heteroepitaxial $Ga_{1-x}In_xP$ growth: The compensator design consists of three elements: (1) ROSKM described by f; (2) filter gains Gi(t) based on nonlinear-filtering techniques; and (3) feedback law K based on dynamical programming.

media composed of ambient/SRL/film/substrate. We model the reflection/refraction of the SRL by an effective medium with the homogeneous dielectric function $\varepsilon_1(t)$ and the thickness $d_1(t)$. Let us denote the four media by the indices $n = 0$, 1, 2, 3 labeled from the ambient to the substrate. The reflection coefficient $r_{n-1,n}$ from the $(n-1)$-st media to nth media is given by

For the formulation of the control problem [73], the multi-layer film stack of $Ga_xIn_{1-x}P$ with different composition x is analyzed using the virtual interface (V-I) method described by Aspnes [1,74,75]. Consider the above formulated four layer media composed of ambient/SRL/film/substrate and replace it through a four media stack that is built up by

- the ambient (0),
- the SRL, represented by (1),
- a the near surface layer (2) describing the growing film with composition x, and
- a virtual substrate (k), represented by its complex virtual reflectance coefficients r_k.

Extending the theory of the virtual interface method [76,77] to a four media stack, the reflectance amplitude r of the p-polarized light is given by

$$rr_4 = \frac{r_{01} + \hat{r}\,e^{-2i\Phi_1}}{1 + r_{01} + \hat{r}\,e^{-2i\Phi_1}} \quad \text{with} \quad \hat{r} = \frac{r_{12} + r_k\,e^{-2i\Phi_2}}{1 + r_{12} + r_k\,e^{-2i\Phi_2}} \tag{3.33}$$

Here, r_{01}, r_{12}, Φ_1, and Φ_2 are functions in $\varepsilon_1(t)$, $d_1(t)$, $\varepsilon_2(t)$ and $d_2(t)$, respectively. The virtual reflection index r_k is updated by

$$r_k = \frac{r_{k,k-1} - r_{k-1}\,e^{-2i\Phi_2}}{1 + r_{k,k-1}r_{k-1}\,e^{-2i\Phi_2}} \quad \text{with} \quad r_k = A_k\,e^{-i\Phi_k} \tag{3.34}$$

at the end of cycle, where θ_k defines the phase factor. The thickness of the grown layer is estimated based on the phase factor. For each homogeneous layer increment we have the estimate of the thickness d_2 by

$$d_2 = \frac{\lambda}{4\pi\sqrt{\varepsilon_2 - \varepsilon_0 \sin^2\varphi_0}}(\theta_{end} - \theta_{begin}) \tag{3.35}$$

where the θ_{end}, θ_{begin} is the phase factor at the end and beginning of the layer. Similarly the growth gr_k per each cycle k can be calculated by

$$gr_k = \frac{\lambda}{4\pi\sqrt{\varepsilon_2 - \varepsilon_0 \sin^2\varphi_0}}(\theta_k - \theta_{k-1}) \tag{3.36}$$

At this point, we can establish a mathematical control-loop, as schematically outlined in Fig. 21, for the control of the deposition process with a control of composition x in the $Ga_xIn_{1-x}P$ surface layer, utilizing the real-time measured PR signals at the two different angles of incidence φ_i, $i = 1{,}2$:

$$R_i(t) = |rr_4|^2 h_i(\varepsilon_1(t), d_1(t), gr(t), x(t) + \text{noise} \tag{3.37}$$

where the output function h_i are determined by (Eqs. (3.33)–(3.36)). The nonlinear filtering algorithms applied for real-time estimates [78] yield the composition x, the growth rate gr(t) and the dielectric function of the surface layer.

It also estimates the concentrations n_k of n_{GaP} and n_{InP} and the accumulated rate constant C_k for the kth GaP and InP cycles from which the input flow rates u^k_{TEG} and u^k_{TMI} are determined by performing a minimization of the cost function

$$\min_{u^k_{TEG}} |(1 + z_k)n^+_{GaP} - gr_d|^2 + \beta|u^k_{TEG} - u^{k-1}_{TEG}|^2, \tag{3.38}$$

$$\min_{u^k_{TMI}} \left|\frac{n^+_{InP}}{n^+_{GaP}} - \frac{z_k}{1 - z_k}\right|^2 + \beta|u^k_{TMI} - u^{k-1}_{TMI}|^2,$$

subject to

$$n^+_{GaP} = e^{-C^k_{TEG}}(n^c_{GaP} - S_{GaP}u^k_{TEG}) + S_{GaP}u^k_{TEG}, \tag{3.39}$$

$$n^+_{InP} = e^{-C^k_{TMI}}(n^c_{InP} - S_{InP}u^k_{TMI}) + S_{InP}u^k_{TMI},$$

respectively. C^k_{TEG} and C^k_{TMI} are the current estimates of C for GaP and InP cycle, and z_k is the desired composition at the k cycle. That is, we control the growth rate by u_{TEG} and then by u_{TMI} the composition for each cycle.

The application of the real-time nonlinear filtering and feed-back control algorithm requires to establishment of the correlation of composition and growth rate dependency as a function of flow-ratio. A series of experiments growing thick epilayers with constant composition x in $Ga_{1-x}In_xP$ were grown and analyzed by XRD to obtain the compositional relationship with the established flow-ratio TMI:TEG. The growth rates were calculated from the interference fringes obtained in the PR signals. Fig. 22 summarizes the results of the ex-situ analysis, showing a nonlinear correlation between growth rate and composition as a function of an established flow-ratio TMI:TEG.

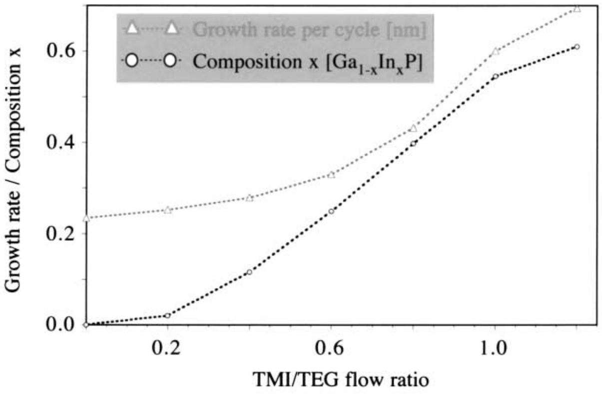

Fig. 22. Composition x and growth rate of $Ga_{1-x}In_x$Pas a function of the TEG:TMI flow-ratio.

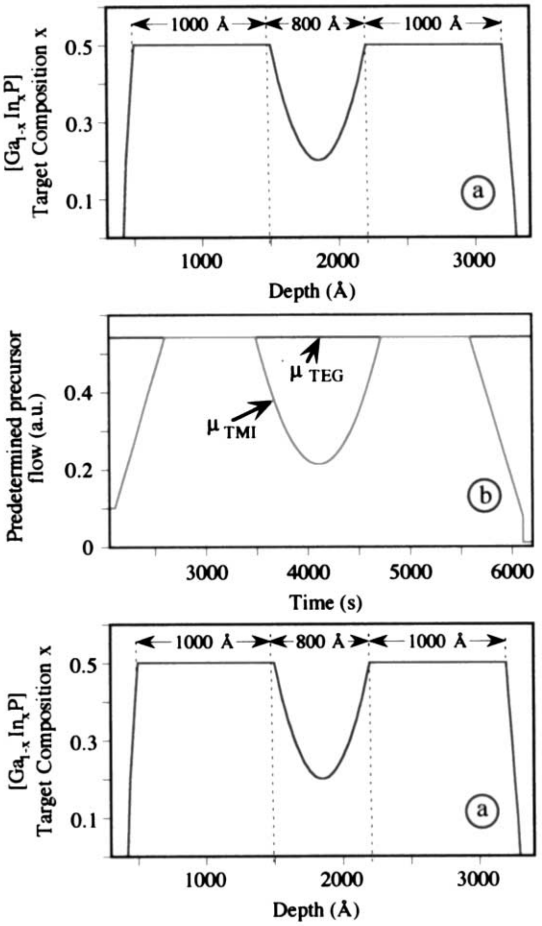

Fig. 23. Open-loop controlled growth of a $Ga_{1-x}In_xP$: (a) target structure; (b) predetermined time-wise flow profile; and (c) SIMS depth profile of grown $Ga_{1-x}In_xP$ heterostructure compared with target profile.

The established correlation between growth rate and composition x with the TMI:TEG flow-ratio is used next to estimate the growth parameter for compositionally graded heterostructures underopen-loop control conditions as well as initial data base for the closed-loop control algorithm. For comparison between open-loop and closed-loop control results, similar target-profiles were designed as schematically shown in Fig. 23a. The target-profile consists of a GaP buffer layer grown on Si, a linear graded $Ga_{1-x}In_xP$ heterostructure, a layer of constant composition $Ga_{0.5}In_{0.5}P$, a parabolic graded $Ga_{1-x}In_xP$ heterostructure, a second layer of $Ga_{0.5}In_{0.5}P$, and a final 100 Å linear graded $Ga_{1-x}In_xP$ heterostructure back to GaP. For open-loop control, a predetermined time-wise flow profile was employed in which the flow of TEG is kept constant and the flow of TMI is varied to match desired composition and thickness, as shown in Fig. 23b. The calculated time-wise flow profile for TEG and TMI was created using the composition to flow-ratio dependency and growth rate to flow-ratio dependency established in Fig. 22. The grown parabolic $Ga_{1-x}In_xP$ heterostructure is analyzed by secondary mass ion spectroscopy (SIMS), the depth profile of which is shown in Fig. 23c.

For SIMS depth profiling, the In^+–Cs and $^{71}Ga^{2+}$–Cs-ion intensities were analyzed. The sputtering rated varied from 2.46 to 4.23 Å/s, with a strong compositional dependency. The compositional dependency was calibrated on $Ga_{1-x}In_xP$ layers with constant composition with compositions measured by XRD.

Accounting for an instrumental broadening of approximately 50 Å and a depth integration of typically 40–50 Å, two errors in the SIMS analysis have to be considered: (a) the integration and instrumental broadening leads to a compositional smear-out of profiles over 100–150 Å and (b) the compositional dependency of the sputtering rate leads to an accumulative error in the depth estimate. The instrumental broadening factor and the given integration time leads to an error in composition, estimated to be about 10%. Even though if all uncertainties in the SIMS depth analysis are considered, the discrepancy between the target profile and measured profile of the parabolic heterostructure are quit large, indicating poor tracking of the target profile under open-loop control conditions.

In the next step, the developed control algorithm is applied to control thickness and composition in multi-

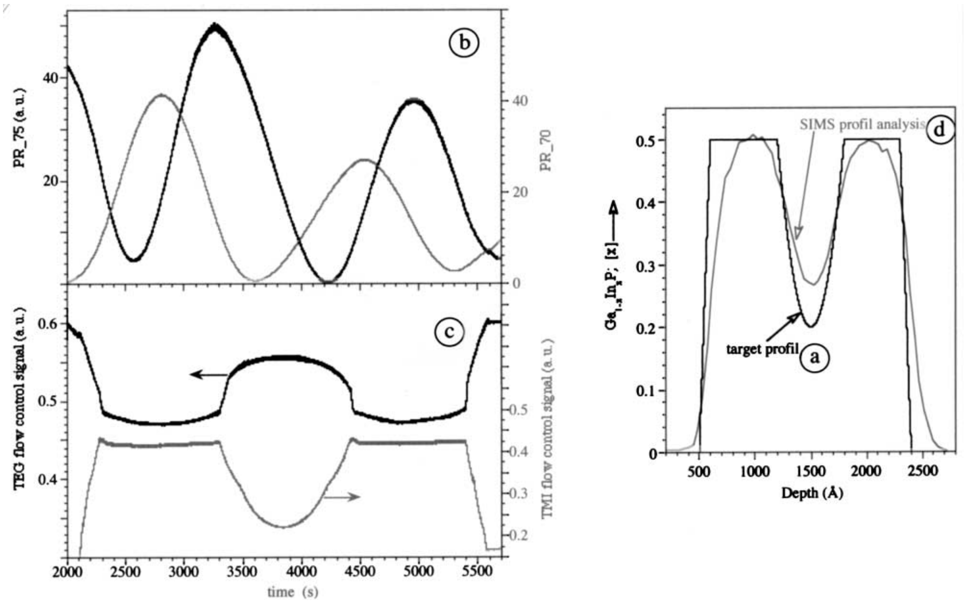

Fig. 24. Closed-loop feed-back control growth of a parabolic graded 600 Å wide $Ga_{1-x}In_xP$ heterostructure embedded in 500 Å thick $Ga_{0.5}In_{0.5}P$ layers on Si(001): (a) target profile; (b) PR signals entering as feed-back control signals in the control algorithm; (c) adjusted TMI and TEG flow signals; and (d) post-growth SIMS profile analysis result.

ple parabolic graded $Ga_{1-x}In_xP$ heterostructures. For this parabolically graded quantum well structures with wells between 200 and 1000 Å have been grown under open- and closed-loop control. The application of the real-time nonlinear filtering and feed-back control algorithm is demonstrated in Fig. 24 using the growth of a 1000 Å wide compositionally parabolic graded $Ga_{1-x}In_xP$ structure as an example. The evolutions of the two PR signals, PR_75 and PR_70 are shown in Fig. 24(b). The real-time updated closed-loop control flow profile is shown in Fig. 24(c). During closed-loop control, variation of the flow of TMI is employed to control composition x while variation in the flow of TEG is used to control the growth rate, as constrained by Eqs. (3.38) and (3.39). The SIMS analysis, shown in Fig. 24(d) together with the target profile show excellent tracking within the uncertainties in the SIMS depth analysis.

Fig. 25 shows the compositional SIMS depth profile for two grown multiple heterostructure, composed of a series of 200 Å parabolic $Ga_{1-x}In_xP$ wells separated by 200 Å of constant composition $x = 0.40$ under closed-loop control. The SIMS analysis of these samples is subject to the compositional smear-out and the accumulative error in sputtering, which accounts for the shallow parabolic compositional structures. However, the comparison with the target profile indicates that the closed-loop feed-back control algorithm maintains excellent profile tracking.

4. Concluding remarks

During the last decades, a variety of optical characterization techniques have been developed with supplementing strength in characterization of particular aspects of properties/insights. Robust and simple techniques may be applicable to improve the reproducibility in standard industrial processes presently used. Past difficulties in numerical analysis of multi-layered compounds can be tackled using readily available computing power in data acquisition, data analysis as well as mathematical modeling. The advantages of real-time process monitoring—compared to post-growth analysis—are overwhelming,

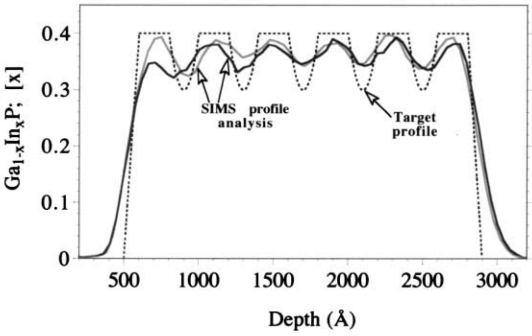

Fig. 25. Closed-loop controlled growth of multiple parabolically graded $Ga_{1-x}In_xP$ hetero-structures, with 200 Å width.

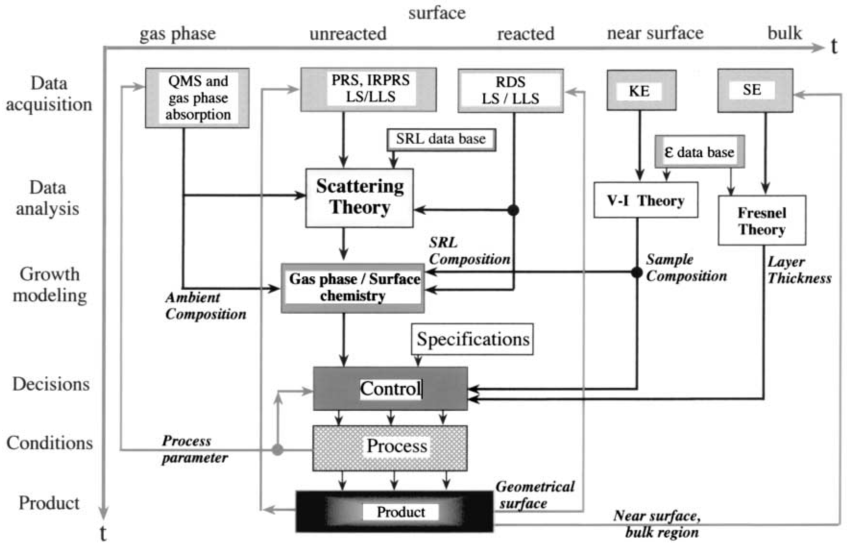

Fig. 26. Real-time monitoring of thin film growth applied in various regions relevant to the growth process.

considering the physical and chemical insights gained and the opportunities opened up for process optimization and control.

The need of more complex characterization techniques with enhanced sensitivity to surface processes will be largely focus to the following areas:

- optimization of existing materials, heterostructures and growth processes,
- generation of precise recipe parameter that can be transferred to industrial processes,
- development of new materials, and
- to gain a better understanding in fundamental physical and chemical processes taken place during nucleation and steady-state growth.

For all these tasks, a combined application of techniques with complementary information is required, as schematically illustrated in Fig. 26. The schematic shows the application of growth monitoring techniques with time increasing along the region axis from left to right and the information axis from top to the bottom. Information about the ambient is accessible by QMS or gas phase absorption spectroscopy, depending on the operation pressure. The unreacted part of on SRL (low-pressure conditions) can be probed by PRS, the reacted part of the SRL by a combination of RDS, PRS and LLS. The near surface dielectric function as well as the bulk dielectric function can be obtained by kinetic-or spectral ellipsometry, and be combined with V-I theory for process control. The analytical modules, scattering theory and surface/gas phase chemistry, deal with the interpretation of the optical data and the modeling of the growth process, respectively. The control module compares the analyzed data, coming from either the surface module or from the V-I module, to target values and adjusts process parameter accordingly.

Acknowledgements

This work has been supported in part by the DOD-MURI Grant F49620-95-1-0447.

References

[1] D.E. Aspnes, Real-time optical diagnostics for epitaxial growth, Surf. Sci. 307–309 (1994) 1017–1027.

[2] J.V. Armstrong, T. Farrell, Real-time monitoring of the growth of AlGaAs layers by dynamic optical reflectivity (DOR), III-Vs Rev. 5 (1992) 40–41.

[3] T. Farrell, J.V. Armstrong, In-situ laser reflectometry of the epitaxial growth of thin semiconductor films, Appl. Surf. Sci. 86 (1995) 582–590.

[4] T. Farrell, J.V. Armstrong, Optical monitoring of the growth of a GaAs/AlGaAs superlattice, Semicond. Sci. Technol. 7 (1992) 1495–1498.

[5] K.P. Killeen, W.G. Breiland, In-situ spectral reflectance monitoring of III–V epitaxy, J. Electron. Mater. 23 (2) (1994) 179–183.

[6] W.G. Breiland, K.P. Killeen, Proc. Mater. Res. Soc. 406 (1995) 99–104.

[7] H. Grothe, F.G. Boebel, J. Cryst. Growth 127 (1993) 1010–1013.

[8] D.E. Aspnes, N. Dietz, Optical approaches for controlling epitaxial growth, Appl. Surf. Sci. 130–132 (1998) 367–376.

[9] D.E. Aspnes, A.A. Studna, Reflectance-difference spectroscopy of (110) GaAs and InP, J. Vac. Sci. Technol. A 5 (4) (1987) 546–549.

[10] D.E. Aspnes, J.P. Harbison, A.A. Studna, L.T. Florez, Reflectance-difference spectroscopy system for real-time measurement of crystal growth, Appl. Phys. Lett. 52 (12) (1988) 957–959.

[11] D.E. Aspnes, R. Bhat, E. Colas, V.G. Keramidas, M.A. Koza, A.A. Studna, J. Vac. Sci. Technol. A 7 (3) (1989) 711–716.

[12] H. Zama, K. Sakai, S. Oda, Jpn. J. Appl. Phys. Part 2 31 (9A) (1992) L1243–L1245.

[13] N. Kobayashi, T. Makimoto, Y. Yamauchi, Y. Horikoshi, In-situ monitoring of gallium arsenide growth process in MOVPE by surface photo-absorption method, J. Cryst. Growth 107 (1–4) (1991) 62–67.

[14] T. Makimoto, Y. Yamauchi, N. Kobayashi, Y. Horikoshi, Jpn. J. Appl. Phys. 29 (2) (1990) L207–L209.
[15] N. Dietz, H.J. Lewerenz, An optical in-situ method for layer growth characterization, Appl. Surf. Sci. 69 (1993) 350–354.
[16] N. Dietz, A. Miller, K.J. Bachmann, Real-time monitoring of homoepitaxial and heteroepitaxial processes by p-polarized reflectance spectroscopy, J. Vac. Sci. Technol. A 13 (1995) 153–155.
[17] N. Dietz, K.J. Bachmann, Real-time monitoring of epitaxial processes by parallel-polarized reflectance spectroscopy, MRS Bull. 20 (1995) 49.
[18] K.A. Bertness, C. Kramer, J.M. Olson, J. Moreland, In-situ observation of surface morphology of InP grown on singular and vicinal (001) substrates, J. Electron. Mater. 23 (2) (1994) 195.
[19] Max Born, Emil Wolf, Principles of Optics, 6th ed., Pergamon, New York, 1980.
[20] R.M.A. Azzam, N.M. Bashara, Ellipsometry and Polarized Light, North-Holland, Amsterdam, ISBN 0-444-87016-4 (1987).
[21] I.P. Herman, Optical Diagnostics for thin Film Processing, Academic Press, New York, 1996.
[22] G. Bauer, W. Richter, Optical Characterization of Epitaxial Semiconductor Layers, Springer, Berlin, 1996.
[23] R.M.A. Azzam, Relationship between the p and s Fresnel reflection coefficients of an interface independent of angle of incidence, Opt. Soc. Am. A 8 (7) (1986) 928–929.
[24] D. Brewster, A treatise on new philosophical instruments, vol. 309, London, 1813.
[25] P.H. Miller, J.R. Johnson, Complex index of refraction of semiconducting surfaces, Physica XX (11) (1954) 1026–1028.
[26] S.P.F.b.t.l. Humphreys-Owen, Comparison of reflection methods of measuring optical constants without polimetric analysis, and proposal for new methods based on the Brewster angle, Proc. Phys. Soc. LXXXVII 5 77, 1961, pp. 949–957.
[27] N. Dietz, H.J. Lewerenz, Simulataneous detection of optical constants ε_1 and ε_2 by Brewster angle reflectivity measurements, Appl. Phys. Lett. 60 (19) (1992) 2403.
[28] H.B. Holl, Specular reflexion and characteristics of reflected light, J. Opt. Soc. Am. 57 (1967) 683.
[29] R.F. Potter, Basic parameters for measuring optical properties, in: E.D. Palik (Ed.), Handbook of Optical Constants of Solids, Academic Press, Washington, DC, 1985, pp. 11–35.
[30] D.E. Aspnes, The accurate determination of optical properties byellipsometry, in: E.D. Palkin (Ed.), Handbook of Optical Constants of Solids, Academic Press, Washington, DC, 1985, pp. 89–112.
[31] U. Rossow, W. Richter, Spectroscopic elliposmetry, in: G. Bauer, W. Richter (Eds.), Optical Characterization of Epitaxial Semiconductor Layers, Springer, Berlin, 1996, pp. 69–128.
[32] W.R. Hunter, Measurement of optical constants in the vacuum ultraviolet spectral region, in: E.D. Palkin (Ed.), Handbook of Optical Constants of Solids, Academic Press, Washington, DC, 1985, pp. 69–88.
[33] M. Elshazly-Zaghloul, R.M.A. Azzam, Brewster and pseudo-Brewster angles of uniaxial crystal surfaces and their use for determination of optical properties, J. Opt. Soc. Am. 72 (1982) 657–661.
[34] T.E. Darcie, M.S. Wahlen, Determination of optical constants using pseudo-Brewster angle and normal incidence reflectance measurements, Appl. Opt. 23 (1984) 1130–1131.
[35] R.M.A. Azzam, E.E. Ugbo, Contours of constant pseudo-Brewster angle in the complex espsiolon plane and analytical method for the determination of optical constants, Appl. Opt. 28 (1989) 5222.
[36] H.J. Lewerenz, N. Dietz, Defect identification in semiconductors by Brewster angle spectroscopy, J. Appl. Phys. 73 (10) (1993) 4975–4987.
[37] O.S. Heavens, Optical Properties of Thin Solid Films, Butterworths, London, 1955.
[38] G.B. Airy, Reflexion an Schichten; Interferenzbeziehungen, Philos. Mag. 2 (1833) 20.
[39] J.D.E. McIntyre, D.E. Aspnes, Surf. Sci. 24 (1971) 417–434.
[40] J.D.E. McIntyre, Optical reflection spectroscopy of chemisorbed monolayers, in: B.O. Serophin (Ed.), Optical Properties of Solids New Developments, North Holland, Amsterdam, 1971, pp. 556–630.
[41] F. Abeles, C. R. Acad. Sci. Paris 228 (1949) 553.
[42] J.C. Kelly, O.S. Heavens, Measurement of refractive index of a transparent film on a refecting substrate, Optica Acta 6 (1959) 339–343.
[43] G. Jungk, Determination of optical constants; a null-method for non-absorbing surface films, Phys. Stat. Sol. A 34 (1976) 69–72.
[44] A. Balzarotti, P. Picozzi, S. Santucci, New method for determining the optical constants by the angular modulation of reflectance, Surf. Sci. 37 (1973) 994–1001.
[45] H. Arwin, I. Lundstroem, A reflectance methodfor quanlification of immunalogical reactions on surfaces, Anal. Biochem. 145 (1985) 106.
[46] H. Arwin, S. Welin, I. Lundstrom, Reflectance method for immunoassay on solid surfaces, in: Ngo, That Tjien (Eds.), Nonisot. Immunoassay, Plenum Press, New York, NY, 1988, pp. 313–330.
[47] N. Kobayashi, Y. Horikoshi, Optical investigation on the growth process of GaAs during migration-enhanced epitaxy, Jpn. J. Appl. Phys. 28 (11) (1988) L1880–L1882.
[48] N. Kobayashi, T. Makimoto, Y. Yamauchi, Y. Horikoshi, Investigation of growth processes in flow-rate modulation epitaxy and atomic layer epitaxy by new in-situ optical monitoring method, Acta Polytech. Scand. Chem. Technol. Metall. Ser. 195 (1990) 139–145.
[49] N. Kobayashi, Y. Horikoshi, Spectral dependence of optical reflection during flow-rate modulation epitaxy of gallium arsenide by the surface photo-absorption method, Jpn. J. Appl. Phys. 29 (1990) L702–L705.
[50] N. Kobayashi, Y. Kobayashi, Y. Yamauchi, Y. Horikoshi, In-situ optical monitoring of the decomposition process of gaseous sources in metal-organic chemical vapor deposition and atomic layer epitaxy, Appl. Surf. Sci. (1992) 0169–4332.
[51] N. Kobayashi, Y. Kobayashi, In situ monitoring and control of atomic layer epitaxy by surface photo-absorption, Thin Solid Films 225 (1992) 32–39.
[52] Y. Horikoshi, M. Kawashima, N. Kobayashi, Optical investigation of gallium arsenide growth process in molecular beam epitaxy and migration-enhanced epitaxy, J. Cryst. Growth 111 (1–4) (1991) 200–204.
[53] K. Hingerl, D.E. Aspnes, I. Kamiya, L.T. Florez, Relationship among reflectance-difference spectroscopy, surface photoabsorption, and spectroellipsometry, Appl. Phys. Lett. 63 (1993) 885–887.
[54] R.M.A. Azzam, Angular sensitivity of Brewster-angle reflection polarizers: an analytical treatment, Appl. Opt. 26 (1987) 2847.
[55] N. Dietz, A. Miller, J.T. Kelliher, D. Venables, K.J. Bachmann, Migration-enhanced pulsed chemical beam epitaxy of GaP on Si(001), J. Cryst. Growth 150 (1995) 691.
[56] N. Dietz, U. Rossow, D. Aspnes, K.J. Bachmann, Real-time optical monitoring of epitaxial growth: pulsed chemical beam epitaxy of GaP and InP homoepitaxy and heteroepitaxy on Si, J. Electron. Mater. 24 (11) (1995) 1571.
[57] K.J. Bachmann, N. Dietz, A.E. Miller, D. Venables, J.T. Kelliher, Heteroepitaxy of lattice-matched compound semiconductors on silicon, J. Vac. Sci. Technol. A 13 (1995) 696.
[58] N. Dietz, K.J. Bachmann, p-Polarized reflectance spectroscopy: a highly sensitive real-time monitoring technique to study surface kinetics under steady state epitaxial deposition conditions, Vacuum 47 (1996) 133.

[59] K.J. Bachmann, U. Rossow, N. Sukidi, H. Castleberry, N. Dietz, Heteroepitaxy of nearly lattice-matched tetrahedrally coordinated compound semiconductors on Si(100), J. Vac. Sci. Technol. B 14 (1996) 3019.

[60] N. Dietz, U. Rossow, D.E. Aspnes, K.J. Bachmann, Real-time optical monitoring of heteroepitaxial growth processes on si under pulsed chemical beam epitaxy conditions, Appl. Surf. Sci. 102 (1996) 47–51.

[61] N. Dietz, U. Rossow, D.E. Aspnes, K.J. Bachmann, Real-time optical monitoring of heteroepitaxial growth processes on si under pulsed chemical beam epitaxy conditions, Appl. Surf. Sci. 102 (1996) 47.

[62] N. Dietz, N. Sukidi, C. Harris, K.J. Bachmann, Real-time monitoring of surface processes by p-polarized reflectance, J. Vac. Sci. Technol. A 15 (1997) 807.

[63] K.J. Bachmann, N. Sukidi, N. Dietz, C. Hoepfner, S. LeSure, H.T. Tran, S. Beeler, K. Ito, H.T. Banks, Real-time monitoring of the kinetics of pulsed chemical beam epitaxy by p-polarized reflectance, J. Cryst. Growth 183 (1998) 323.

[64] N. Dietz, N. Sukidi, C. Harris, K.J. Bachmann, Real-time monitoring of heteroepitaxial $Ga_xIn_{1-x}P$/GaP Growth by p-polarized reflectance, Conf. Proc. IPRM-9'97, ISSN 1092-8669, 1997, p. 521.

[65] K.J. Bachmann, C. Hoepfner, N. Sukidi, A.E. Miller, C. Harris, D.E. Aspnes, N. Dietz, H.T. Tran, S. Beeler, K. Ito, H.T. Banks, U. Rossow, Molecular layer epitaxy by real-time optical process monitoring, Appl. Surf. Sci. 112 (1997) 38.

[66] N. Dietz, K. Ito, Real-time optical characterization of GaP heterostructures by p-polarized reflectance, Thin Solid Films 313–314 (1998) 615.

[67] K.J. Bachmann, S. Mahajan, Evaluation of initial stages of heteroepitaxial growth by reflectance spectroscopy and transmission electron microscopy, in: O. Auciello, A. Kraus (Eds.), In-situ Real-Time Characterization of Thin Film Growth, Processing and Phenomena, Wiley, New York, NY, 1998.

[68] A.J. Murrell, A.T.S. Wee, D.H. Fairbrother, N.K. Singh, J.S. Foord, G.J. Davies, D.A. Andrews, J. Cryst. Growth 105 (1990) 199.

[69] J.T. Kelliher, K.J. Bachmann, Chemical beam epitaxy of gallium phosphide using triethylgallium and tertairybutlyphosphine, Mater. Res. Soc. Symp. Proc. 282 (1992) 51.

[70] S.H. Li, C.A. Larsen, N.I. Buchan, G.B. Stringfellow, W.P. Kosar, D.W. Brown, J. Appl. Phys. 65 (1989) 5161–5165.

[71] G.H. Fan, R.D. Hoare, M.E. Pemble, I.M. Povey, A.G. Taylor, J.O. Williams, J. Cryst. Growth 124 (1992) 49–55.

[72] K.J. Bachmann, U. Rossow, N. Dietz, Real-time monitoring of heteroepitaxial growth processes on the silicon (001) surface by p-polarized reflectance spectroscopy, Mater. Sci. Eng. B 37 (1–3) (1995) 472–478.

[73] V. Woods, K. Ito, I. Lauko, N. Dietz, Real-time thickness and compositional control of $Ga/1-x/In/x/P$ growth using p-polarized reflectance, J. Vac. Sci. Technol. A18 (2000) 1190–1195.

[74] D.E. Aspnes, Minimal-data approaches for determining outer-layer dielectric responses of films from kinetic reflectometric and ellipsometric measurements, J. Opt. Soc. Am. A 10 (1993) 974–983.

[75] D.E. Aspnes, Minimal-data approaches for determining outer-layer dielectric responses of films from kinetic reflectometric and ellipsometric measurements, Appl. Phys. Lett. 62 (4) (1993) 343–345.

[76] D.E. Aspnes, IEEE J. Selected Top. Quantum Electron. 1 (1995) 1054–1063.

[77] D.E. Aspnes, Optical approaches to determine near-surface compositions during epitaxy, J. Vac. Sci. Technol. A 14 (1996) 960–966.

[78] K. Ito, K. Xiong, New Gaussian filter for nonlinear filtering problems, IEEE Trans. Automat. Control (2000) 910–927.